Sedimentology and isotope geochemistry of transitional evaporitic environments within arid continental settings: From erg to saline lakes

Ross P. Pettigrew[1], Charlotte Priddy[1], Stuart M Clarke[1], Matthew R. Warke[2], Eva E. Stüeken[2] and Mark W. Claire[2]

[1] Basin Dynamics Research Group, School of Geography, Geology and the Environment, Keele University, England, UK, ST5 5BG

[2]School of Earth & Environmental Sciences, University of St Andrews, St Andrews, Scotland, UK, KY16 9AL

Short Title – Transitional evaporitic environments

ABSTRACT

Arid continental basins typically contain a spectrum of coeval environments that coexist and interact from proximal to distal. Within the distal portion, aeolian ergs often border playa, or perennial, desert lakes, fed by fluvial incursions or elevated groundwaters. Evaporites are common features in these dryland, siliciclastic dominant settings. However, sedimentary controls upon evaporite deposition are not widely understood, especially within transitional zones between coeval clastic environments that are dominantly controlled by larger scale allocyclic processes, such as climate. The sulphur ($\delta^{34}S$) and oxygen ($\delta^{18}O$, $\Delta^{17}O$) isotope systematics of evaporites can reveal cryptic aspects of sedimentary cycling and sulphate sources in dryland settings. However, due to the lack of sedimentological understanding of evaporitic systems, isotopic data can be easily misinterpreted. This work presents detailed sedimentological and petrographic observations, coupled with $\delta^{34}S$, $\delta^{18}O$ and $\Delta^{17}O$ data, for the early Permian Cedar Mesa Sandstone Formation (western USA). Depositional models for mixed evaporitic /

clastic sedimentation, which occurs either in erg-marginal or lacustrine-marginal settings, are presented to detail the sedimentary interactions present in terms of climate variations that control them. Sedimentological and petrographical analysis of the evaporites within the Cedar Mesa Sandstone Formation reveal a continental depositional environment and two end member depositional models have been developed: erg-margin and lake-margin. The $\delta^{34}S$ values of gypsum deposits within the Cedar Mesa Sandstone Formation are consistent with late Carboniferous to early Permian marine settings. However, a marine interpretation is inconsistent with sedimentological and petrographic evidence. Consequently, $\delta^{34}S$, $\delta^{18}O$ and $\Delta^{17}O$ values are probably recycled and do not reflect ocean-atmosphere values at the time of evaporite precipitation. They are most likely derived from the weathering of older marine evaporites in the hinterland. Thus, the results demonstrate the need for a combination of both sedimentological and geochemical analysis of evaporitic systems to better understand their depositional setting and conditions.

Keywords: Aeolian, Cedar Mesa Sandstone, gypsum, playa lakes, $\Delta^{17}O$, $\delta^{34}S$

INTRODUCTION AND BACKGROUND

Dryland continental basins typically contain a spectrum of depositional environments from alluvial fans and immature fluvial systems within the proximal region (e.g. Blissenbach, 1954; Hooke, 1967; Bull, 1977; Blair & McPherson, 1994; Harvey *et al*, 2005; Parsons & Abrahams, 2009), through to aeolian and arid-fluvial systems within the medial (e.g. Langford, 1989; Langford & Chan, 1989; Herries, 1993; Veiga *et al.*, 2002; Cain & Mountney, 2009; Al-Masrahy & Mountney, 2015; dos Reis *et al.*, 2019; Formolo Ferronatto *et al.*, 2019, Priddy & Clarke, 2020), and playa lake or lacustrine environments within the distal region (Tunbridge, 1984; Huerta *et al.*, 2010). In the medial to distal regions of many dryland continental basins, evaporite deposits are typically recognized along shallow lacustrine margins (Carter & Pickerill, 1985; Orti *et al.*, 2003; Orti *et al.*, 2007), where they may form a distinct depositional setting in their own right, or are dispersed within erg-marginal and ephemeral-fluvial settings (Kocurek, 1988; Porter, 1986; Blakey, 2000; Clemmenson *et al.*, 2000; Tanner & Lucas, 2007). However, evaporite deposits are not limited to only the distal regions within continental basins. Ancient

evaporite deposits have been described from proximal regions, typically deposited in association with springs or alluvial fans in settings characterized by active tectonism and rapid subsidence (Southgate *et al.*, 1989; Fischer & Roberts, 1991; Helvaci, 1995), and many modern examples, such as the acid saline lakes of Western Australia, are deposited in topographic lows on cratons (e.g Aerts *et al.,* 2019).

The preserved clastic sediments of medial to distal aeolian and arid lake-marginal basinal settings are recognized for their potential to act as high-quality hydrocarbon reservoirs or aquifers within the subsurface (e.g. Glennie *et al.,* 1978), but interdigitated fluvial sediments are known to have detrimental effects upon reservoir performance (e.g. North & Prosser, 1993). Consequently, the evolution of mixed arid clastic systems, and the preservation of the sediments they deposit, have been well documented (e.g. Langford & Chan, 1989; Herries, 1993; Veiga *et al.,* 2002; Mountney & Jagger, 2004). However, the same cannot be said for mixed evaporitic–clastic systems of arid continental basins. Despite strong associations between clastic and evaporitic environments, and between the deposits they produce, evaporitic settings and their sediments are typically studied independently from the coeval siliciclastic systems (Denison *et al*, 1998;). Few studies examine the interdependence of one setting upon the other and the complex sedimentary interactions between them. The studies that have addressed this issue focus on the geochemistry and hydrology of the system (e.g. Huerta *et al.,* 2010) or look purely at the sediments (e.g. Benison & Goldstein 2000; Gündogan *et al.,* 2005). Rarely do these studies take a holistic interdisciplinary approach necessary for a complete understanding of these systems. This is despite the obvious implications that inter-dispersed clastic sediments have upon the economic potential of evaporitic deposits themselves, or the detrimental impacts that inter-dispersed evaporitic sediments have upon clastic reservoirs and aquifers (Warren, 1999, 2006).

Evaporites can preserve geochemical proxies for palaeoenvironmental conditions, palaeoclimate and evidence of past life that are typically absent from, or poorly preserved in, the siliciclastic deposits of arid coeval settings. These include proxies for: palaeo-water and palaeo-air temperatures (Kovalevich, 1975; Petrichenko, 1979; Lowenstein & Spencer 1990; Goldstein & Reynolds, 1994; Roberts & Spencer, 1995; Benison & Goldstein, 1999), ancient water chemistry (Horita *et al.,* 2002; Lowenstein

et al., 2005) and atmospheric oxygenation (Blamey *et al.*, 2016; Blättler *et al.*, 2018, Crockford *et al.*, 2019).

The triple oxygen isotope ($\Delta^{17}O$) record, preserved in sedimentary sulphates, can be used to constrain the coupled evolution of the biosphere and the atmosphere over a geological timescale (Crockford *et al.*, 2016; 2019) and may be the only geochemical proxy of atmospheric change (Bao, 2015). Tropospheric oxygen (O_2) possesses a mass-independent, negative $\Delta^{17}O$ value, which is inherited from ozone creation and destruction reactions in the stratosphere (Thiemens, 2006). The magnitude of the negative $\Delta^{17}O$ value in tropospheric O_2 depends upon atmospheric composition (CO_2 and O_2 concentrations), as well as levels of gross primary productivity (Yung *et al.*, 1991; Crockford *et al.*, 2018). Detailed geochemical modelling can be used to deconvolve which factors principally control the atmospheric $\Delta^{17}O$ value over Earth history (e.g. Waldeck *et al.*, 2019), but all approaches rest on the assumption that the $\Delta^{17}O$ preserved in sedimentary sulphates is representative of the time period in question.

The $\Delta^{17}O$ value of atmospheric oxygen is transferred to the sulphate anion complex during oxidative sulphide weathering (Killingsworth *et al.*, 2018). It has been estimated that *ca* 21 to 34% of the oxygen atoms in sulphate are derived from atmospheric O_2 (Kohl & Bao, 2011), although other estimates place this as high as 60% (see Waldeck *et al.*, 2019, and references therein) and as low as *ca* 7% (Thurston *et al.*, 2010). Once formed, the sulphate complex does not readily undergo oxygen isotope exchange with other fluids, other than under highly acidic, or high pressure/temperature, conditions (Kusakabe & Robinson, 1977; Chiba *et al.*, 1981). As such, it is non-labile and considered to be stable through relatively shallow, low-temperature diagenesis (Bao, 2015).

Oxygen isotope exchange with water, however, does occur as a result of microbial sulphur cycling, which is prevalent in the marine (Turchyn & Shrag, 2004) and, as is being increasingly recognized, in the continental realm (Benison & Bowen, 2013; Johnson *et al.*, 2015). Although previous studies have focused mainly on tracking sulphur through microbial sulphur cycling, the fate of sulphate-bound oxygen – particularly any mass-independent $\Delta^{17}O$ signal it may carry – during sulphide oxidation and

101 microbial sulphate cycling has been a more recent development (Hemingway *et al.*, 2020). Although
102 sulphates precipitated from marine waters do carry a significant negative $\Delta^{17}O$ value, due to the
103 propensity of microbial cycling in the marine realm, it is generally acknowledged that the $\Delta^{17}O$ value
104 preserved by marine sulphates is a conservative estimate of the true, atmospheric $\Delta^{17}O$ value of the time
105 period (Crockford *et al.*, 2019).

106 The fluvial sulphate flux constitutes the sole input into marine sulphate reservoirs (Halevy *et al.*, 2012),
107 is derived from the oxidative weathering of pyrite (incorporating a contemporaneous atmospheric $\Delta^{17}O$
108 signal) and dissolution of older calcium sulphates (Halevy *et al.*, 2012; Wortmann & Paytan, 2012).
109 Thus, in order to use $\Delta^{17}O$ values to infer temporal changes in coupled atmosphere–biosphere evolution,
110 it is necessary to minimise the spatial variability in $\Delta^{17}O$ preservation as far as possible. As such,
111 continental, dryland evaporite sequences could prove an important inventory of atmospherically derived
112 $\Delta^{17}O$.

113 This study investigates the environmental, spatial and temporal relationships between evaporitic and
114 clastic sediments within the arid and dominantly clastic continental settings preserved within the Cedar
115 Mesa Sandstone Formation, south-eastern Utah, USA. It describes and interprets multi-scale
116 relationships between evaporitic and clastic sediments using an outcrop lithofacies analysis augmented
117 by petrographic and XRD data. Triple oxygen and sulphur isotope analyses, conducted on evaporite
118 samples, provide further insight into possible depositional controls upon the system and demonstrate
119 the value of examining evaporitic deposits in the context of their coeval clastic setting. Generic
120 depositional models that account for the observations within a clastic–evaporitic depositional setting
121 are developed, from which the possible larger scale allocyclic controls and their effects upon the
122 preserved deposits are discussed.

123 GEOLOGICAL SETTING AND PREVIOUS WORK

124 The early Permian (Cisuralian) Cedar Mesa Sandstone Formation of the Western USA was deposited
125 within the Paradox Basin: an oval shaped, Carboniferous flexural foreland basin formed by loading in

response to the uplift of the Ancestral Rocky Mountains (ARM), and defined in shape by the depositional extent of the evaporites of the Paradox Formation (Mallory, 1960; Condon, 1997; Barbeau, 2003).

Exposed across much of southern Utah (Fig. 1), the dominantly clastic sediments of the Cedar Mesa Sandstone Formation form part of a 4 km thick late Pennsylvanian to mid-Permian basin fill that was derived principally from the Uncompahgre Uplift of the Ancestral Rocky Mountains that were present to the north-east of the basin (Loope, 1984). The age of the formation is given by U-Pb detrital zircon studies (Dickinson & Gehrels, 2003), vertebrate fossils and trackways (Lockley & Madsen Jr, 2008; Gay *et al.*, 2020) and lateral and vertical relationships with other formations and coeval deposits that can be dated from well constrained palaeontological data (Condon, 1997; Lucas & Krainer, 2005). Originally described as the deposits of an aeolian system (McKnight, 1940; Baker, 1946), the formation was later reinterpreted to be of shallow marine origin from the presence of broken shell fragments in the cross-stratification (Baars, 1962; 1979; Mack, 1977; 1979). However, from grainfall–grainflow couplets that form foresets of large-scale cross-stratification (Loope, 1984), and from further continental indicators including rhizoliths (Stanesco & Campbell, 1989), an aeolian origin for the sediments was reaffirmed by the 1980s (Loope, 1984) and is widely accepted today (Lanford & Chan, 1989; Mountney & Jagger, 2004).

The Cedar Mesa Sandstone Formation is one of four lithostratigraphical units that comprise the Cutler Group in the distal portion of the Paradox Basin. The oldest unit of the Cutler Group – the lower Cutler beds – is an informal lithostratigraphical subdivision that comprises aeolian, fluvial and shallow marine sediments (Jordan & Mountney, 2010) related to repeated cyclic transgressions driven by alternations between an arid and humid climate (Jordan & Mountney, 2012). The lower Cutler beds are overlain conformably by the predominantly wet aeolian sediments of the Cedar Mesa Sandstone Formation (Mountney & Jagger, 2004), that are, in turn, conformably overlain by the terminal fluvial fan sediments of the Organ Rock Formation (Cain & Mountney, 2009). Finally, aeolian sediments of the De Chelly Sandstone form the youngest division of the Cutler Group in the distal parts of the basin (Blakey, 1996; Dubiel *et al.*, 1996; Condon, 1997; Stanesco *et al.*, 2000).

To the north-east of the basin (Fig. 1A), sediments of the Cedar Mesa Sandstone Formation have a complex interfingering relationship with coeval sediments of the Cutler Group that were shed south-westerly into the basin from the Uncompaghre Uplift to form proximal to medial alluvial fan and fluvial deposits (Mack, 1977; Mountney & Jagger, 2004). To the north-west of the basin, aeolian sediments of the Cedar Mesa Sandstone interfinger with shallow-marine limestone indicating the location of the palaeoshoreline (Fig. 1) (Loope, 1984).

The aeolian sediments of the Cedar Mesa Sandstone represent the deposits of a north-east – south-west trending coastal erg system that developed along the shoreline, and was supplied with sediment sourced from the local marine shelf (Loope, 1984; Blakey, 1988; Blakey *et al.*, 1988). The erg extended 100 km south, with sediments of the erg centre preserved 130 km west of Blanding near Hite (Fig.1), in south-eastern Utah (Langford & Chan, 1993; Mountney, 2006). Major flooding surfaces that are preserved in the aeolian strata to the south-east of Canyonlands National Park (Fig.1) subdivide the erg sediments as the dune-fields became progressively smaller and more isolated away from the erg centre (Langford & Chan, 1989). Major dune field sediments of the erg are separated by the sediments of wet interdunes, which grade into sabkha-like evaporitic deposits towards the south-east (Fig.1) (Blakey, 1988; Blakey *et al.*, 1988; Peterson, 1988; Condon, 1997; Huntoon *et al.*, 2000; Mountney & Jagger, 2004; Langford & Massad, 2014; Pettigrew *et al.*, 2019).

Sabkha-like evaporitic deposits of the Cedar Mesa Sandstone Formation are exposed around the town of Bluff in south-eastern Utah. They show sedimentary features including nodular evaporites and enterolithic growth structures interbedded with aeolian sands and fine-grained clastic sediments. These strata have been interpreted as the product of deposition in inland sabkhas associated with playa lakes of the coeval aeolian erg (e.g. Glennie, 1972), but sulphur isotope values ($\delta^{34}S$) of gypsum from the succession fall within the narrow marine range of Permian $\delta^{34}S$ values (Claypool *et al.*, 1980; Stanesco & Campbell, 1989) and suggest a marine influence on the depositional environment. However, carbon ($\delta^{13}C$) and oxygen ($\delta^{18}O$) analysis of limestones within the succession only partly fall within the common marine range (Hudson, 1977). Consequently, the evaporitic sediments of the Cedar Mesa Sandstone were interpreted to be the product of a sabkha environment that was, in part, fed by marine

waters via unspecified methods, with mixing of fresh and marine waters under conditions of intense evaporation (Stanesco & Campbell, 1989).

Recent work suggests an environment isolated from marine waters (Langford & Massad, 2014; Pettigrew *et al.,* 2019), based on abundant evidence of freshwater vegetation and mud cracks (Langford & Massad, 2014) and distinct carbonate microfacies of continental origin (Pettigrew *et al.*, 2019). The carbonate microfacies are interpreted to have formed due to microbial processes within either arid or humid aeolian interdunes, saline pans around the edge of desert lakes, and in, or around, an inland evaporitic lake that showed evidence of periodic contraction and expansion (Pettigrew *et al.,* 2019).

METHODS

Ten detailed sedimentary logs were measured through canyons running perpendicular to the strike of the sediments at approximately 3 km intervals along a 15 km long north – south transect. No subsurface core exists for the study area. The logs have a cumulative sediment thickness of 7.5 km and form the basis of the lithofacies within this study. A further two logs (one 60 km to the south of Bluff, and one 100 km to the north of the town) were measured to show the spatial variability in sediments preserved, and to provide regional context. The logs were correlated to one another using the top and base of the Cedar Mesa Sandstone Formation as markers, and by tracing prominent units between logs using continuous outcrop.

From log 1.4 (Road Canyon), in the middle of the study area (Figs 1 and 2), evaporites were sampled from every evaporitic bed, and from nodules and veins within clastic deposits. The mineralogy of these samples was characterized using X-Ray diffraction (XRD), and triple oxygen and sulphur isotope analyses were conducted upon them. A further ten evaporitic samples were collected from logs 1.4 to 1.8 and were cut dry to produce 30 μm thick, unstained thin sections that were subsequently examined for evaporitic textures.

Samples for X-Ray Diffraction (XRD) analyses were milled to a fine powder using an agate ball mill. The XRD analyses were performed at the University of St Andrews using a Philips PW1830

Diffractometer (Co Kα X-ray source), Philips PW1710 Diffractor Control unit, and operating conditions of 30 kV and 30 mA (Koninklijke Philips N.V., Amsterdam, The Netherlands). Samples were scanned from 3 to 70° 2θ using a step size of 0.01° and a counting time of 1 second per step.

The extraction and purification of sulphate for stable isotope analysis is described fully in the Supplementary Information. Measurements of $\delta^{34}S$ (Table. 3) were made from SO_2 gas using a Thermo FlashSmart Elemental Analyser (EA) combined with a MAT 253 isotope-ratio mass spectrometer (IRMS; Thermo Fisher Scientific, Waltham, MA, USA) at the University of St Andrews (Warke *et al.*, 2020). SO_2 was generated by combustion of barite samples (0.14 –0.19 mg) and vanadium pentoxide powder (1–2 mg) combustion in the presence of O_2 at 1020°C. SO_2 was separated from other gases using a Gas Chromatography (GC) column after combustion products were carried via helium stream through tungsten oxide catalysts and copper wire (to reduce excess O_2) and a magnesium perchlorate trap (*ca* 20°C) to remove water. Sample isotopic compositions were calibrated to Vienna Canyon Diablo Troilite (V-CDT) scale by bracketing barite samples with the international reference standards IAEA-SO5, IAEA-SO6 and NBS-127, and are reported in the standard delta notation where:

$$\delta^{34}S = 1000 * [(({}^{34}S/{}^{32}S)_{sample} / ({}^{34}S/{}^{32}S)_{V\text{-}CDT}) -1] \quad (1)$$

Long-term analytical uncertainty is better than 0.3‰ (1σ).

Triple oxygen isotope analysis was performed using a laser fluorination method at the OASIC laboratory at Louisiana State University (LSU). The protocol is described elsewhere (e.g. Crockford *et al.*, 2018) and is outlined fully in the Supplementary Information. Sample gases were measured with respect to internal standard LSU-O_2 which is calibrated to Standard Mean Ocean Water (SMOW). Long-term analytical uncertainty is better than 0.05‰ (1σ). Measurements of $\delta^{17}O$ and $\delta^{18}O$ were made on purified O_2 using a duel inlet MAT 253 isotope-ratio mass spectrometer (IRMS) and are presented in the standard delta notation where:

$$\delta^{X}O = 1000 * [(({}^{X}O/{}^{16}O)_{sample} / ({}^{X}O/{}^{16}O)_{SMOW}) -1] \quad (2)$$

In Eq. 2, 'x' can equal 17 or 18. $\Delta^{17}O$ values were calculated from $\delta^{17}O$ and $\delta^{18}O$ values where:

$$\Delta^{17}O = 1000 * [\ln(1+\delta^{17}O/1000) - (0.528 * \ln(1+\delta^{18}O/1000))] \quad (3)$$

As the laser fluorination method causes a mass-dependent fractionation, $\delta^{18}O$ values were separately evaluated by converting barite to CO gas at 1450°C using a Thermal Conversion Elemental Analyzer (TCEA). Measurements of $\delta^{18}O$ (Table 3) were made on CO gas using a MAT253 IRMS (isotope ratio mass spectrometer; Thermo Fisher Scientific, Waltham, MA, USA) at the OASIC laboratory at LSU. Long-term analytical uncertainty on $\delta^{18}O$ is better than 0.5‰ (1σ) (Peng *et al.*, 2011).

RESULTS

Lithofacies analysis of logged sections (Fig. 2) reveal fifteen lithofacies deposited by subaqueous, sub-aerial and evaporitic processes that form commonly occurring deposits typical of the arid environment. Log data for evaporitic lithofacies are augmented with results of XRD analysis and thin-section observations. The XRD data are summarized in Table 1 and discussed in the text, with all XRD spectra shown in the Supplementary Information (Appendix). The distinctive features of each of the fifteen lithofacies and their interpretations are summarized in Table 2. They have been grouped into nine discrete facies associations based on the dominant depositional process and deposits preserved, each of which is described in detail below.

Aeolian deposits

Dune associations (AD)

Deposits within the study area are composed of laterally extensive tabular bodies with relatively flat basal bounding surfaces. Lateral extents are over tens of metres, although stratigraphic thicknesses are limited (*ca* 5 m). Deposits of this type are dominantly composed of tabular cross-bedded sandstones (Sxb) with planar foresets (1 to 5 cm in thickness), and rare occurrences of trough cross-bedded sandstones (Stxb) with tangential foresets of similar thickness (1 to 5 cm) (Fig. 3A). The deposits lack large-scale set or coset development, with sets 1 to 5 m and cosets no greater than 10 m in thickness. Planar cross-bedded and trough cross-bedded sets typically interfinger with inversely graded, ballistic-rippled sandstone (Sxr), structureless sandstone (Sm) and gypsum facies (G) along the toesets of the

foresets, with small-scale (<50 cm) soft-sediment deformation also a typical feature. The foresets are sporadically disturbed by evaporite deposits in the form of nodules and veins (Fig. 3B).

Interpretation:

Cross-bedded sandstones that display tangential foresets, formed of lamination couplets of structureless to reverse graded sandstone with a thin veneer of finer grained sandstone, represent aeolian dune deposits formed by alternating grainfall and flow processes. This indicates reasonably well developed dune-forms with lee-slope slip-faces close to, or at, the angle of repose (Hunter, 1977; Kocurek, 1981; 1991; 1996; Langford & Chan, 1989; Mountney, 2006). Dunes were dominantly straight-crested transverse forms, preserving planar cross-bedded sets with planar set-bounding surfaces. Sporadically, sinuous-crested transverse forms developed, or straight-crested forms broke up or evolved into sinuous-crested bedforms under autogenic processes, due either to changes in migration rate, sediment supply or wind direction (Rubin & Hunter, 1984). The presence of ballistic wind ripples interfingering with the toesets of cross-bedding suggests the presence of dune plinths upon which ballistic ripples dominated. Soft-sediment deformation, typically preserved near the base of the deposits, indicate dunes migrated in the presence of a water table close to, or at, the surface (McKee *et al.*, 1971; Doe & Dott, 1980; Horowitz, 1982; Mountney & Thompson, 2002). The presence of gypsum preserved along the base of foresets or toeset surfaces, indicates that solute-rich water was drawn up preferential flow pathways in the sediments of the advancing dune as a result of capillary action.

Sandsheet associations (SH)

Deposits of this type consist of thin, sheet-like, laterally extensive, tabular bodies with flat basal and top surfaces. The deposits have lateral extents over distances greater than tens of metres with limited thicknesses (1 to 2 m), and consist primarily of inversely graded, ballistic-rippled (Sxr) (Fig. 3C and D) or structureless sandstones (Sm), with sporadic crudely developed cross-bedded sandstones (Sxb). Deposits typically grade laterally and vertically into dune and interdune deposits and contain gypsum nodules and veins that deform the bases of the deposits.

Interpretation:

Deposits primarily composed of ballistic-ripple strata (Sxr) or structureless sandstones (Sm) indicate aeolian sandsheets in which limited grain-size variations do not distinguish the bounding surfaces of individual cross-laminated sets (Kocurek, 1981). The sandsheets developed under conditions where sediment supply was insufficient for full-scale dune development (Kocurek & Nielson, 1986; Biswas, 2005), resulting in only minor crude cross-bedding. Soft sediment deformation indicates a water table close to the surface, with deformation resulting from water table fluctuations and loading of the sandsheet by the following dune deposits (McKee *et al.*, 1971).

Standing water deposits

Interdune associations (ID)

Deposits of this type consist of either lensoidal bodies that pinch out over distances of less than one metre, or tabular bodies with larger lateral extents over tens of metres. In each case, thicknesses are no greater than 2 m. Deposits comprise structureless sandstones (Sm), oscillatory current rippled siltstone and sandstone (Swr) and sand-rich carbonates (Lsm). Deposits grade vertically and laterally into dune (AD) and sandsheet (SH) deposits, with sporadic examples occurring in relationship with ponded water (PA) and displacive gypsum (DG) associations. Rhizoliths, bioturbated sediment and mottling are present throughout (Fig. 4C), with sporadic occurrences of convolute-bedded sandstone (Scu), gypsum/anhydrite nodules and efflorescent crusts.

Interpretation:

Associations of this type are interpreted as the deposits of wet and saline interdunes. Carbonate deposits have accumulated in long-lived shallow ponds of standing water above the depositional surface, close to an aeolian dune field that supplied clastic sediment to the interdune (Loope 1981; 1984; Langford & Chan, 1989; Pettigrew *et al.*, 2019). The isolated nature of the deposits signifies laterally restricted interdunes developing in an enclosed or semi-enclosed setting, either as a result of floodwaters trapped between surrounding sinuous-crested dunes, or by rises in the water table in topographical depressions (Loope, 1984; Purvis 1991; Mountney & Jagger, 2004). Oscillatory-ripples are formed from wind shear over the shallow water of the interdune setting (Martell & Gibling, 1991). Rhizoliths and mottling

indicate the short-lived presence of water at the surface, probably as a result of fluctuations in the elevation of the water table.

Ponded waters associations (PA)

Deposits of this type are characterized by laterally extensive (>10 m) tabular bodies with planar basal surfaces, but thicknesses are highly variable, with deposits ranging between 0.2 to 10 m thick. Deposits are composed primarily of sandstones displaying symmetrical oscillatory-ripples (Swr) (Fig. 4B), fine-grained carbonates (Lm) with sporadic rounded gypsum nodules and minor parallel-laminated siltstones (Ssl). Ponded water sediments typically grade vertically and laterally into interdune (ID), unconfined flow (UF) and suspension settlement (SS) deposits. Rhizoliths, bioturbated sediment, mottling and gypsum nodules are typical features. The rhizoliths are horizontal to sub-vertical and the bioturbated sediment consists of thin (<10 cm) branched vertical and horizontal tube-like burrows.

Interpretation:

A dominance of wave-ripple sandstones and fine-grained carbonates suggests a shallow ponded water setting. Wave-ripples have been generated by wind shear across the water surface (Martell & Gibling, 1991) to produce symmetrical ripples. Fine-grained carbonate facies suggest variations in clastic content and prolonged conditions of low-energy standing water (Tucker, 1978; Platt & Wright, 1991 Pettigrew *et al.*, 2019) with frequent reworking by wave action. The low diversity of fossil species within the carbonates, coupled with gypsum nodules, suggests an arid, highly saline and probably restricted environment (Cecil, 1990; Flügel, 2004), with the development of rhizoliths indicating surface stabilization around edges of long-standing quiet water bodies (Platt & Wright, 1991; Owen *et al.*, 2008).

Stratified waters/suspension settlement associations (SS)

Deposits of this type comprise laterally extensive tabular bodies with planar basal surfaces. Lateral extents are commonly over tens of metres whereas stratigraphic thicknesses range from 1 m to tens of metres, with the thickest deposits present in the southern portion of the study area (Figs 1C and 8). The deposits are dominantly composed of black to purple coloured siltstones to very fine-grained sandstones

(Ssl) (Fig. 4A) intercalated sporadically with oscillatory-rippled sandstones (Swr) (Fig. 4B), fine-grained carbonates (Lm) and horizontally-laminated pedogenic facies (Sfo) (Fig. 4D). The siltstones are typically structureless, mottled, with a sporadically high organic content. Deposits grade laterally into pedogenic facies (Sfo) and typically grade vertically with unconfined flow (UC), or ponded water (PA) deposits.

Interpretation:

Fine-grained siltstones that lack internal sedimentary structures indicate deposition in lakes that were perennial and of greater extent than Ponded Water or Interdune settings, and in which the sediments settled mostly from suspension (Fielding, 1984; Tanner & Lucas, 2007). Sporadic evidence for high organic content within siltstones could indicate depths sufficient enough to cause thermal stratification (Boehrer & Schultze, 2008). Intermittent intercalation with wave-ripples (Swr) shows a shallowing of the water level, potentially caused by climate fluctuations, and an increasing influence from wind shear (Martell & Gibling, 1991). The occurrence of horizontally laminated pedogenic facies suggests stabilization around the margins of a long-standing body of water (Eberth & Miall, 1991).

Flowing water deposits

Unconfined flow associations (UF)

Deposits of this type consist of thin, sheet-like, laterally extensive bodies with relatively flat to slightly concave-upward, erosional, basal surfaces. Lateral extents are highly variable and range from 1 m to tens of metres, which often branch into thinner sheet-like units, and vertical extents are no greater than 1.5 m. This association comprises cross-bedded sandstones (Sfxb) with sporadic mud clasts, arranged into multiple low-angle cross-bedded sets (Fig. 4E) (up to 1 m thick), planar laminations (Sfpl) of 0.5 to 1.0 cm thick (Fig.4F) and sporadic climbing-ripple laminated sandstone (Sfrl). Preservation of the full, fining upward succession is rare and the association often grades into suspension settlement siltstones, ponded water deposits or pedogenic facies.

Interpretation:

The flat erosional bases, laterally extensive geometries and sedimentary fill of these associations represents characteristic non-channelized flow incorporating either splay-type or sheetflood-type architectures (Tunbridge, 1981; Sneh, 1983; Stear, 1985; Miall, 1985; North & Davidson, 2012; Priddy *et al.*, 2019; Priddy & Clarke, 2020). A dominance of low-angle cross-bedding and planar-laminated sandstones that stack into fining upward vertical successions indicates a transition from lower-flow regime to upper-flow regime conditions and structures, within high velocity flows that waned quickly (Bridge, 1993; Mitten *et al.*, 2020), whereas thin units that split and branch represent the margins of individual sheetfloods as a result of a rapid reduction in depth associated with an ephemeral, sand-rich sheet flood (Miall 1985; 1996).

Chemically precipitated deposits

Bedded gypsum/anhydrite associations (BG)

Deposits of this type have a flat basal surface, and consist of thin, flat bodies. Observed lateral extents are variable, ranging between 0.5 to 5.0 m with vertical extents typically less than 5 m. The deposits consist almost entirely of white to peach (5R 8/3), very fine-grained, crystalline gypsum (G), with outcrop-scale alabastrine and porphyroblastic textures resembling white marble, interbedded with thin beds of siltstones (Ssl). The evaporitic sediments are crudely bedded with sporadically laminated layers of peach coloured elongate gypsum crystals and large botryoidal gypsum nodules (up to 50 cm in height) which bifurcate up from a stem and branch into a cauliflower-like appearance (Fig. 5A). They comprise a matrix of alabastrine gypsum with very minor amounts of anhydrite and quartz. Three distinct textures are recognized: (i) randomly organized angular gypsum (<1 mm) surrounded by brown mudstone clasts, with frequent veins filled with satin spar gypsum (Fig. 5B); (ii) spherical and sub-rounded patches of sand (gypsum and some quartz) (Fig. 5C); and (iii) thin (<1 to 3 mm) undulating beds of bladed gypsum with vertical textures and rare swallowtail crystal morphology (Fig. 5B and C).

The bedded gypsum deposits (BG) grade vertically and laterally into suspension settlement (SS), ponded waters (PA) and displacive gypsum (DG) deposits, and occur sporadically in association with unconfined flow (UF) and interdune (ID) deposits.

Interpretation:

These deposits result from the accumulation of primary gypsum and anhydrite by precipitation in shallow, saline waters (Kendall, 1981; Handford, 1991; Warren, 1991) where modern studies indicate that the three textures observed are typically present together (Benison *et al.*, 2007). Laminated layers with elongate crystals are indicative of selenite, signifying bottom-growth of crystals within standing brines (Benison & Goldstein, 2000, Benison & Goldstein, 2001). Selenite has been dehydrated to anhydrite during burial diagenesis and rehydrated to secondary gypsum during exhumation (Gundogan *et al.*, 2005). Siliciclastic sediment intercalated with the bedded evaporite crystals indicates coeval clastic deposition by either fluvial, lacustrine or aeolian processes (Foster *et al.*, 2014).

Displacive gypsum/anhydrite associations (DG)

These deposits consist of thin undulating bands of laterally extensive bodies with undulating basal and top bounding surfaces. Lateral extents range from 1 m to tens of metres and thicknesses range from 0.5 to 2.0 m. The deposits are dominantly composed of crystalline gypsum (G) with alabastrine and porphyroblastic textures, and minor amounts of anhydrite, celestine and quartz (Table 1) (Fig 6B to D). The evaporites comprise a matrix of interlocking alabastrine crystals (<1 mm) with randomly orientated large (1.5 to 4.0 mm) cubic to sub-cubic halite crystals filled with a clear cement with bladed cement crystals present along the edges (Fig. 6E). Small gypsum nodules (up to 20 cm in thickness) and laminated-bands of enterolithic convoluted folds (Fig. 6C and D), polygonal hummocks (Fig. 6A) and chicken-wire structures (Fig. 6B) are common features within these deposits. The nodules are interbedded either with thin beds (up to 20 cm thick) of pastel blue, very fine to fine-grained, parallel-laminated gypsum-bound sandstone (Gspl) within a gypsiferous matrix and cement, or with very fine to fine-grained pedogenic (Sfr) facies with frequent gypsum nodules and veins.

The displacive gypsum (DG) deposits grade vertically and laterally into bedded gypsum (BG) suspension settlement (SS), ponded waters (PA) deposits, and typically occur in association with unconfined flow (UF) and interdune (ID) deposits.

Interpretation:

Interbedded gypsum-bound sandstone with intercalated gypsum nodules and veins relate to saline pan and saline mudflat deposition along the margins of saline lakes (Lowenstein & Hardie, 1985). Enterolithic and chicken-wire structures indicate very early diagenetic (synsedimentary) displacive growth of anhydrite nodules which were partly or completely hydrated to secondary gypsum under post-depositional conditions (i.e. early and/or late diagenesis) and the exhumation process (Butler, 1970). Polygonal hummocks form tepee structures due to desiccation of saline waters and fracturing of salt crusts into polygonal shapes (Warren, 2016), the presence and preservation of such structures suggests a calm, low-energy environment (Lokier & Steuber 2008; 2009). The matrix textures (Fig. 6E) suggest that the host sediment that was originally mud (potentially gypsum-rich mud) with early diagenetic displacive halite crystals. The largest halite crystals (Fig. 6E) show euhedral cubic to sub-cubic habits and are randomly oriented within the finer matrix. The displacive halite crystals appear to have been dissolved (Casas & Lowenstein, 1989; Benison *et al.*, 2015), forming crystal moulds that were later filled with anhydrite or gypsum bladed cement crystals along the edges. The remainder of the crystal mould has been filled with a clear halite cement. The interlocking crystal mosaic present within the fine matrix indicates that the original mud underwent neomorphism.

Brecciated gypsum/anhydrite associations (BrG)

These deposits consist of thick laterally extensive (up to 10 m) lensoidal bodies with flat to undulating basal surfaces. Observed thicknesses range from 1 to 5 m and deposits of this type are especially prevalent at the top of the formation. The deposits are composed almost entirely of weathered mounds (Fig. 7A and B) of white to peach, very fine-grained brecciated gypsum (G) with minor anhydrite (Table 1), and minor components of arid pedogenic facies (Sfr), carbonates (Lm) and gypsum-bound sandstone (Gspl). The matrix of the gypsum deposits is composed of elongate rectangular selenite crystals with rounded ends (1 to 10 mm in horizontal thickness) (Fig.7C). Carbonate deposits are thin (<40 cm) and show wavy laminations, typically interbedded with thin (<20 cm) deposits of gypsum-bound sandstone (Gspl). Pedogenic facies are also typically thin (<50 cm) with frequent gypsum nodules and veins. Deposits of this type (BrG) occur in vertical and lateral relationship with dune (AD) and sandsheet (SH) deposits.

Interpretation:

Brecciated gypsum deposits are interpreted as gypsum dunes resulting from the deflation of gypsum sediment formed in lacustrine and playa lakes during more humid climatic conditions (Szynkiewicz *et al.*, 2010). During the onset of more arid conditions, desiccation of these playa lakes led to the formation of microbial mats, present in the form of carbonate laminations (Pettigrew *et al.*, 2019). Aeolian reworking of desiccated lake beds produced gypsiferous dune deposits controlled by a near-surface groundwater table (Szynkiewicz *et al.*, 2010) and arid soils (Sfr) around lake edges (e.g. Lawton & Buck, 2006). The weathered appearance of the gypsum dunes results from their poor consolidation compared to their clastic counterparts and is a post-depositional burial, dissolution and compaction that destroyed primary bedding fabrics, (Fenton *et al.*, 2014). The dune sediment matrix shows characteristics of aeolian deposits of gypsum/anhydrite that have been slightly altered by diagenesis (hydration–dehydration reactions) and that compare with morphologies of modern gypsum sand dunes and sand flats, such as those at White Sands in New Mexico, in the Rio Grande Rift (Wilkins & Currey, 1997; Anderson *et al.*, 2002; Langford, 2003; Kocurek *et al.*, 2007; Szynkiewicz *et al.*, 2010) and the Olympia Undae Dune Field (Mars) (Langevin *et al*, 2005; Fishbaugh *et al.*, 2007).

Spatial distribution of deposits

Spatial analysis of the deposits indicates a general increase in the relative proportion of 'water derived' deposits southward over the study area (Fig. 8). In the north, logs 1.0 to 1.3 (covering a transect approximately 60 km long from Canyonlands to the south of US95) demonstrate dominantly aeolian deposits of dune and sandsheet, with subordinate interdunes, and indicate a dry to sporadically damp setting throughout times when deposition of the Cedar Mesa was controlled by aeolian processes. South of US163, log 1.9 demonstrates dominantly lacustrine deposits of suspension settlement and unconfined flow associations and indicates a perennial lake throughout Cedar Mesa times. From US163 northward for approximately 30 km (logs 1.4 to 1.8; the central part of the studied area), the Cedar Mesa contains aeolian and standing water deposits mixed with chemically precipitated and flowing water deposits in varying proportions, showing the interbedded and competing nature of the aeolian and lacustrine settings.

DEPOSITIONAL SETTINGS

Dry and saline sandflats

In the north of the study area between Canyonlands and Blanding (logs 1.0 to 1.3) (Fig. 2), thick accumulations of dune associations (AD) and laterally extensive sandsheet (SS) deposits dominate the successions, with minimal accumulations of evaporitic associations. Whereas, in the rest of the study area, between Blanding and Bluff (logs 1.4 to 1.8), the deposits of aeolian dunes (AD) are small, isolated, typically evaporite-rich, haloturbated and interbedded with evaporate-rich interdunes (ID) and arid palaeosols that typically display evaporite nodules, gypsum veins and efflorescent crusts.

A dominance of dune and sandsheet associations in the north (Canyonlands to Blanding) suggests deposition in a dry sandflat setting most probably at the edge of the main Cedar Mesa erg. Dune deposits lack salt influence and are comparatively larger than those in the south with trough cross-bedding arranged into multiple sets and cosets. Limited interdune and sandsheet deposits are preserved between dune sediments (Mountney & Jagger, 2004; Vackiner *et al.,* 2011; Antrett, 2013).

However, between Blanding and Bluff, the deposits represent a saline sandflat environment, sometimes referred to as a wet aeolian or saline aeolian sabkha (Warren, 2016). Small isolated dunes migrated over saline saturated ground waters, with a saline water table in contact with, or above, the depositional surface (Driese, 1985; Warren, 2016; Zuchuat *et al.*, 2019). The deposits of the saline sandflats show varying degrees of salt preservation, however haloturbation is typical, even where little capillary salt is preserved (Warren, 2016). Overprinting by extensive disruptive evaporite crystal growth can modify or destroy primary depositional features (Ahlbrandt & Fryberger, 1981; Warren, 2016) which typically consist of subaqueous current and wave ripples, wavy and contorted bedding, adhesion structures, bioturbation, desiccation cracks, megapolygons (Warren & Kendall, 1985), deflation surfaces and wind-ripple lamination (Martin & Evans, 1988; Goodall *et al.*, 2000; Mountney & Thompson, 2002; Warren, 2016).

Wet interdune/arid outwash plain

This setting is characterized by thick deposits of ponded water (PA) and interdune (ID) associations interbedded with minor occurrences of unconfined flow (UF), stratified waters (SS) and dune associations (AD). Dune deposits are typically straight crested (Sxb) and interbedded laterally and vertically with interdune deposits of massive sandstone (Sm), oscillatory current rippled sandstone (Swr) and rooted palaeosols (Sfr).

These deposits represent a wet interdune/arid outwash plain. Sporadic occurrences of dune deposits separated from one another by wide interconnected wet interdunes suggests a setting with a degree of aridity but limited aeolian sediment supply, such as at the edge of larger dune field. These areas typically have higher water tables during humid periods, forming ponded water deposits and carbonates (Pettigrew *et al.*, 2019). Occasional higher energy events input clastic material through unconfined flows to interdune areas reworking sediment (Howell & Mountney, 1997; Mountney, 2006).

Perennial lake

This setting is characterized by thick stratified water associations (SS) primarily comprising deposits of siltstone (Ssl) interbedded with lacustrine carbonates (Lm and Lsm), oscillatory current rippled sandstone (Swr) and palaeosols (Sfo) with sporadic unconfined flows (UF).

These deposits thicken towards the south and indicate a regionally-extensive low-energy, shallow lacustrine setting influenced by the sporadic input of sand-rich water from unconfined surface run off. Organic rich siltstones indicate relative longevity and sufficient depths of a perennial lake for thermal stratification. Wave ripples suggest periods of lake level fluctuations as shallowing water levels increased the influence of wind shear and/or wave action reworking along the margins of the lake (Bridge & Demicco, 2008). The lake margin deposits grade into humid palaeosols indicating stabilization around the lake edge.

Ephemeral saline lake-saline pan/mudflat

The deposits of ephemeral saline lakes are characterized by bedded gypsum (BG) with minor, laterally restricted deposits of the ponded water (PA) associations which grade into displacive (DG) and brecciated gypsum (BrG) associations of a saline pan/mudflat.

This setting represents saline pan and mudflat environments with ephemeral saline lakes which formed during arid periods via the evaporation and desiccation of previously long-lived lakes. In the main submerged areas of the lake, during desiccation (Lowenstein & Hardie, 1985) the earliest precipitates nucleate as thin rafts of connected platy euhedral cumulate halite crystals at the water–air interface that are held by surface tension until they grow too large and sink (Schreiber & Kinsman, 1975; Castens-Seidell, 1984; Last, 1984; Alderman, 1985; Hardie *et al.*, 1985; Lowenstein & Hardie, 1985; Smoot & Lowenstein, 1991). As evaporation of the lake progresses, salts are concentrated in the remaining water to form smaller ephemeral saline lakes in which sulphate and calcium concentrate in shallow waters. This facilitates the precipitation of bottom-nucleating, vertically-elongated gypsum crystals (e.g. Kendal, 1978; Last, 1984; Smoot & Lowenstein, 1991). The fibrous/prismatic gypsum grows perpendicularly to the substrate in contact with the brine (bottom-growth) (Kendall & Harwood, 1996). These crystals increase in size and gradually became a mosaic, formed by displacive growth in very shallow water and/or in the capillary fringe-groundwater zone, as a result of either a fall in water levels or subaerial exposure (e.g. Warren, 2006). Complete desiccation of the saline lake produces polygonal fractures in the salt pan that typically fill with detrital evaporitic or clastic sediment. They preserve as efflorescent crusts (Smooth & Castens-Seidell, 1994) with crack fills, or so-called ‘tepee structures’ where the fill incorporates displacive evaporites (Warren, 1983; Lowenstein & Hardie, 1985; Lokier & Steuber, 2009).

Saline mudflats form in dominantly emergent settings and are characterized by fine-grained clastic sediments, typically clay minerals such as montmorillonite and illite (Brooks & Ferrell, 1970). These sediments are deposited by settlement following influxes of sediment-laden floodwater into shallow ephemeral lakes. With lake contraction, the sediments are exposed. Saline mudflats have little (if any) vegetation and have a saline groundwater table only centimetres to tens of centimetres below the surface

538 which may fluctuate up and down in response to climate. Variations in ground water levels and
539 circulation promote subsurface phreatic evaporite growth as random crystals or nodules, or as
540 concentrated thick layers, displacing surrounding sediment to form chickenwire and enterolithic
541 structures (Smoot & Lowenstein, 1991; Boggs & Boggs, 2009; Warren, 2016). On the surface of the
542 mudflats, precipitation from the evaporation of saline ground waters forms efflorescent evaporites,
543 either as powdery undulating surfaces or as hard crystalline crusts (Smoot & Lowenstein, 1991; Warren,
544 2016). Subaerial exposure and desiccation of gypsum in the vadose zone results in fractures and the
545 reworking of fragments by water inflow (Kendall & Harwood, 1996; Abrantes Jr *et al.*, 2016).

546 # SUMMARY DEPOSITIONAL MODELS

547 Two models showing the intermediate environments between a desert erg and desert lake have been
548 distilled from the depositional settings. Within each model, clear variations in sedimentology and
549 characteristics of more humid or more arid conditions can be recognized (Fig. 9).

550 **Dune-dominant, erg-marginal system**

551 During times of relatively higher humidity, the erg-marginal system is characterized by a wet, marginal,
552 aeolian erg interacting with unconfined run off (e.g. Mountney & Jagger, 2004) that feeds small saline
553 lakes and interdunal areas (Fig. 9). Evaporite development was limited, with sufficient surface water
554 for vegetation and soil formation.

555 Throughout subsequent arid periods accompanied by a drop on the groundwater table, aeolian dunes
556 increased in magnitude and frequency as they became contiguous with the central erg. They formed
557 dune fields, dominated by straight-crested dunes evolving through time into sinuous-crested forms with
558 well-developed dune plinths, within dry sandflats. The facies belt graded distally into a saline sandflat
559 setting, in which small-scale, sinuous-crested, aeolian dunes migrated over saline-rich damp or wet
560 interdunal areas. Locally the solute-rich substrate allowed for the direct precipitation of evaporites and
561 carbonates, intercalated with aeolian calibre clastic sediments, to form saline interdune deposits.
562 However, evidence for the evaporitic nature of the system as a whole is limited primarily to displacive

563 gypsiferous nodules and haloturbation in aeolian bedforms. A wet solute-rich substrate severely limited
564 sediment supply to dunes and consequently led to isolated barchanoid duneforms with laterally
565 interconnected saline interdunes.

566 Although water played a role in the formation of sediments within the erg-margin, the dominant
567 sediment transport processes are wind-driven. Fluctuations in the availability of water at the surface
568 during arid-humid cycles probably resulted from oscillations in the water table, rather than from
569 sustained surface flow from outside the system that fed significant and long-standing bodies of water.

570 **Lake-marginal system**

571 At a time of relatively higher humidity, the lacustrine-marginal system is characterized by the
572 dominance of lacustrine deposits (Fig. 9). A thick lacustrine succession, which predominantly settled
573 from suspension, is interbedded with either surface run off or carbonate sediments depending on the
574 rate of water input and the magnitude of its clastic load. Around the lake margins, any aeolian dunes
575 were small-scale, barchanoid and strongly isolated between sheetflood-like deposits of fluvial origin
576 and vegetated overbank.

577 During subsequent periods of relatively higher aridity, the lake contracted until extensive saline pans
578 and mudflats developed over the edges of the lacustrine depression, associated with the development of
579 localized ephemeral saline lakes. In the lake, the lack of clastic input from unconfined surface run off
580 during periods of increased aridity is coupled with the concentration of dissolved salts as the water
581 evaporated. This led to the deposition of evaporitic sediments dominated first by halite rafts, formed on
582 the lake surface, and later by bottom nucleating gypsum. Enterolithic and displacive salts grew around
583 the edges of the evaporitic lake due to capillary and phreatic growth from the infiltration of saline
584 groundwater, forming pervasive saline mudflats. Finally, subaerial exposure and desiccation of saline
585 cumulates led to the formation of polygonal growth structures coupled with reworking of cumulates by
586 wind-action into aeolian-gypsum dunes. Aeolian dunes deposits are limited despite the increased
587 aridity. Surface and enterolithic mineral growth in these areas severely limits the exposed sediment that

588 is available for aeolian transport, and traps much wind-blown sediment on damp surfaces.
589 Consequently, the dune field shows little to no growth as the lacustrine environment dried out.

590 SULPHUR ($\Delta^{34}S$) AND TRIPLE OXYGEN ($\Delta^{17}O$) ISOTOPE
591 RESULTS

592 In Log 1.4, measured sulphate $\delta^{34}S$ values range from +13.4 ± 0.3‰ to +14.5 ±0.3‰, $\delta^{18}O$ values range
593 from +12.8 ± 0.5‰ to +16.69 ± 0.5‰, and values of $\Delta^{17}O$ range from -0.27 ± 0.05‰ to -0.06 ± 0.05‰
594 (Table 3, Fig. 10). There is no clear relationship between gypsum facies and either $\delta^{34}S$, $\delta^{18}O$ or $\Delta^{17}O$
595 values. In the case of $\Delta^{17}O$ values, some of the most negative values identified occur in veins. There is
596 no clear stratigraphic variation in $\Delta^{17}O$ values (Fig. 10). In the lower portion of Log 1.4 (approximately
597 0 to 20 m; n = 5) $\delta^{34}S$ and $\Delta^{17}O$ values co-vary with less negative $\Delta^{17}O$ values corresponding to less
598 negative $\delta^{34}S$ values (Fig. 10). Throughout the rest of the section, however, there is no discernible
599 covariation between $\delta^{34}S$ and $\Delta^{17}O$ values.

600 Stratigraphic variation in $\delta^{34}S$ can be only tentatively identified given the *ca* 1‰ range in the dataset,
601 which is small in comparison to the error margins on each measurement. However, two shifts from
602 relatively larger to smaller $\delta^{34}S$ values can be visually identified between 0 m and 55 m ,and also
603 between 55 m and 104 m (Fig. 10). These upward trends in $\delta^{34}S$ values are matched by similar trends
604 in $\delta^{18}O$ values which decrease gradually over the same intervals (Fig. 10).

605 Interpretation of isotopes

606 A coupled and gradual upward decrease in $\delta^{34}S$ and $\delta^{18}O$ values suggests the existence of at least two
607 evaporative cycles within the logged section, with the decreasing values reflecting Rayleigh
608 fractionation effects within a closed system (Raab & Spiro, 1996). In such a scenario it seems likely
609 that some freshening of the closed system occurred at *ca* 55 m. Above *ca* 55 m, $\delta^{34}S$ and $\delta^{18}O$ values
610 return to those seen at *ca* 0 m (Fig 10). These trends, however, can only be tentatively identified as the
611 $\delta^{34}S$ values at the base and top of the lower cycle (0 to 55 m) are within error of one another (Fig. 10).
612 There is more distinction in the upper cycle, but the range of $\delta^{34}S$ values remains <1.1‰ (Fig. 10). The

613 $\delta^{18}O$ profile of Log 1.4 mirrors the trends in $\delta^{34}S$ but values at the top and bottom of each cycle are,
614 considering error, distinct from one another.

615 The mean $\delta^{34}S$ value of 14.0‰ (n = 28 ; 1σ = 0.3) is broadly in accordance with the marine $\delta^{34}S$ curve
616 during the early Permian, or late Carboniferous periods (Fig. 11A; Claypool *et al.*, 1980; Kampschulte
617 & Strauss; 2004). Therefore, the simplest interpretation of the $\delta^{34}S$ values in Log 1.4 is that they
618 represent precipitation of gypsum from marine waters. Such an interpretation has been favoured by
619 previous workers (Stanesco & Campbell, 1989).

620 It is important to note that mass-independently fractionated isotopic signatures, like $\Delta^{17}O$ within
621 sedimentary sulphate, are not affected by mass-dependent processes – like evaporation – unless the
622 sulphate anion complex is disturbed, for example in microbial sulphate reduction (Bao *et al.*, 2015). In
623 such cases, any non-zero $\Delta^{17}O$ value would be erased. Although the range of $\Delta^{17}O$ values is
624 comparatively small (*ca* 0.21‰) with respect to the range of $\delta^{34}S$ values, such values are typical of
625 evaporitic sulphates that preserve an atmospheric signal inherited from tropospheric O_2 and imparted to
626 sulphate during sulphide oxidation. For the purposes of comparison, modern tropospheric O_2 has a $\Delta^{17}O$
627 of -0.47‰ (Pack *et al.*, 2017) but the authors would expect only a fraction of that signal (i.e. *ca* 21 to
628 34%) to be transferred to sulphate during sulphide oxidation (Kohl & Bao, 2011). The only processes
629 known to cause mass-independent fractionation of oxygen isotopes and generate negative $\Delta^{17}O$ values
630 in atmospheric O_2 are ozone creation and destruction reactions (Thiemens, 2006). The $\Delta^{17}O$ values
631 measured here, which are as low as -0.27‰, show an unambiguous atmospheric signature.

632 There are relatively few measurements of Phanerozoic $\Delta^{17}O$ values, but most studies to date have
633 focused on Cambrian and Permian marine and non-marine evaporites (Bao, 2005; Bao *et al.*, 2008)
634 reflecting the uneven distribution of evaporites over time (Warren, 2016). Published Permian $\Delta^{17}O$
635 values range anywhere from +0.02 to -0.16‰ (n = 26) and are restricted to the mid to late Permian
636 Period (Bao, 2005; Bao *et al.*, 2008); there are no noted measurements from the early Permian Period.

637 Hence, the negative $\Delta^{17}O$ values measured in the Cedar Mesa Sandstone Formation: (i) show an
638 unambiguous atmospheric fingerprint within sulphate; and (ii) are some of the most negative $\Delta^{17}O$

values measured in the Permian Period, and in the Phanerozoic Eon in general. The measurements herein, therefore, could provide important new insight into the temporal variability of $\Delta^{17}O$ over the Phanerozoic. However, it is important that the source and age of the sulphate complex analysed is accurately known with respect to the age of the sulphate-hosting formation, as discussed below.

DISCUSSION

Lithofacies analysis of outcrop, augmented by thin section and XRD analyses, suggest a fully continental setting for the evaporite-rich sediments of the Cedar Mesa sandstone in the vicinity of Bluff, Utah. Deposition occurred within a transitional zone between a well-established aeolian erg and a saline lake, with the dominance of one depositional setting over the other controlled by variations in aridity. A continental interpretation for the deposits is further supported by the recent published work of Langford & Massad (2015) and Pettigrew *et al.* (2019).

However, isotopic analyses of evaporitic samples collected for this study suggest a marine influence upon deposition of these sediments. The range of measured $\delta^{34}S$ values (+13.4 to +14.5‰) fall within error of late Carboniferous to early Permian marine values (i.e. $+14.6 \pm 0.7$‰; Kampschulte & Strauss, 2004) despite a distinct lack of lithofacies relationships and fossil content that typify successions affected by marine influence or seawater incursions. This apparent conflict between the geochemical and sedimentological data of this study, and the implications for interpreting erg-marginal evaporitic depositional settings in general, are discussed in following sections.

Isotopic signatures: continental or marine?

Interpreting the isotopic signatures within evaporites is typically problematical due to recycling of marine signatures (see Taberner *et al.*, 2000), lack of petrographic analyses to assess the impact of diagenesis, and the use of isotopic values from continental gypsum deposits to construct seawater curves (see Denison *et al*, 1998). The presence of halite and/or gypsum is not an indicator of marine environments or parent waters, although some workers now use those same curves to attribute a marine origin to halite/gypsum. There is a wide range of $\delta^{34}S$ and strontium isotope ($^{87}Sr/^{86}Sr$) values within

saline lakes, with values that overlap with seawater signatures. Benison & Bowen (2013) reported $\delta^{34}S$ values from 17.0 to 20.4 within modern saline lakes in Western Australia, compared to modern seawater $\delta^{34}S$ values of 20.3(±0.3)‰. Therefore, although $\delta^{34}S$ values derived for this study overlap with the marine curve, this does not necessarily imply that they precipitated from seawater. It is, therefore, inaccurate to use only the isotopes from evaporite minerals to infer marine influence and interpret ancient seawater chemistry if it cannot independently demonstrate (for example, through macro-facies and micro-facies analysis) that the depositional setting has experienced marine incursions.

Another possibility that explains the observed $\delta^{34}S$ values equally well is that the sulphate in the gypsum facies has been recycled from an older marine evaporite deposit (Palmer *et al.,* 2004). This requires that there is a suitable unit in the hinterland. In the case of the Cedar Mesa Sandstone, this may be the late Pennsylvanian (*ca* 311 to 306 Ma) Paradox Formation (Trudgill, 2011) which contains abundant deposits of marine evaporites (Nuccio & Condon, 1996) and may have been exposed during deposition of the Cedar Mesa.

Evaporites within the Paradox Formation possess a $\delta^{34}S$ value of +13.3‰ (n = 1; Claypool *et al.,* 1980). Other studies, with larger datasets, have estimated that similarly aged marine evaporites would be likely to have $\delta^{34}S$ values ranging from +14.6(±0.7) to +15.1(±1.7)‰ (n = 26; Kampschulte & Strauss, 2004). The mean $\delta^{34}S$ value measured in this study, +14.0‰ (1σ = 0.4‰; n = 28), lies between the two and within error of both late Carboniferous and early Permian evaporites and marine evaporites of similar age to the Paradox Formation (Kampschulte & Strauss, 2004) (Fig. 11A).

Thus, it is not sufficient to argue, on the basis of ambiguous sulphur isotope values, that evaporites in the Cedar Mesa Sandstone Formation were deposited following marine incursions as has been previously proposed (Stanesco & Campbell, 1989). There are no macro-facies or micro-facies evidence supporting marine influence, and significant evidence arguing against it. The most parsimonious explanation, that reconciles the sedimentological, stratigraphic and isotopic evidence, is that the sulphate within the early Permian Cedar Mesa Sandstone Formation was derived from the dissolution of the older marine evaporites of the late Carboniferous Paradox Formation. Additionally, the recycling

690 of sulphate from the older Paradox Formation may explain why $\delta^{34}S$ and $\Delta^{17}O$ values in the Cedar Mesa
691 Sandstone Formation show no systematic stratigraphic trend or relationship with climatic condition
692 and/or facies.

693 **Controls on deposition, tectonics versus climate**

694 In the absence of marine input to explain the presence of evaporitic strata of the Cedar Mesa Sandstone,
695 other controls upon their deposition should be considered. Tectonics and climate are the primary
696 controls on continental depositional systems (Vail *et al.,* 1991; Quigley *et al.,* 2007), controlling both
697 the type and amount of sediment supplied to the basin and the rate at which accommodation is created
698 and filled (Vail *et al.,* 1991). Tectonic activity creates elevated landscapes, as well as generating
699 structural lows and depocentres, while climate influences the discharge and sediment availability.
700 Tectonic and thermal subsidence are recognized as primary controls on sabkha/playa lake formation by
701 generating tectonic sagging in which water can pool and subsequently evaporate (e.g. Mertz & Hubert,
702 1990).

703 However, deposition of the Cedar Mesa Sandstone Formation coincided with a reduction in the
704 subsidence rate of the Paradox Basin, and thus an accompanying reduction in the rate at which
705 accommodation space was generated. A maximum of approximately 2.7 km of sediment was deposited
706 at an estimated sedimentation rate 84 m/Myr by the end of the Pennsylvanian Epoch (Huntoon *et al.,*
707 1996; Nuccio & Condon, 1996). By contrast, approximately 1.8 km of sediment was deposited at a rate
708 of 40 m/Myr during the Permian Period that overfilled the basin. (Huntoon *et al.,* 1996; Nuccio &
709 Condon, 1996; Condon, 1997; Barbeau, 2003). The overfilled state resulted in a basinward progradation
710 of facies belts due to limited accommodation space (Mountney & Jagger, 2004). This may indicate that
711 basin-scale tectonics had negligible effect on the preserved deposits, acting only as a means of
712 generating accommodation through a relatively constant subsidence rate.

713 Glacio-eustatic processes have been recognized as a driving mechanism for the controls on the central
714 and marginal erg deposits of the Cedar Mesa Sandstone (Mountney & Jagger, 2004) where twelve
715 separate erg sequences can be identified within the aeolian sediments (Mountney, 2006). The sequences

716 reflect 412 kyr Milankovitch eccentricity cycles, which forced cyclic changes in climate (Mountney,
717 2006). It follows that the Cedar Mesa Sandstone was probably influenced by periods of humid–arid
718 climate variations during the early Permian Period, which resulted in periods of contraction and
719 expansion within the lacustrine system in the south of the study area (Figs 8 and 9). Arid climatic
720 intervals led to the development of saline mudflats associated with ephemerally saturated carbonate
721 ponds and saline pans in the south of the study area, and the development of aeolian features
722 predominantly in the north. The presence of diagenetic halite (Fig. 6E) is an indirect proxy for saltier
723 and drier conditions than have previously been attributed to the depositional environment and
724 palaeoclimate of the Cedar Mesa, and is consistent with age-equivalent rocks elsewhere in western
725 equatorial Pangea (Parrish, 1993; Kessler *et al.,* 2001; Ricardi-Branco, 2008; Tabour *et al.,* 2013;
726 Falcon-Lang *et al.,* 2015).

727 Despite a probable dominance of climatic controls upon deposition of sediments of the Cedar Mesa
728 Sandstone, the influence of localized structure upon the position of evaporite deposits within the basin
729 cannot be fully discounted. Large-scale and deep-seated faults of Pre-Cambrian age that bound the study
730 area, and that have been purported to be active during Permian times (Kelley, 1955; Huntoon, 1993;
731 Davis, 1999; Mynatt *et al.,* 2009; Hilley *et al.,* 2010), may have produced localized lows into which
732 surface water was focused to produce wetter conditions, even during arid climatic phases, in which erg-
733 marginal evaporitic environments developed (Pettigrew *et al.,* 2019). It is also not beyond the realms
734 of imagination to suggest that displacement on these faults may have brought older marine
735 Carboniferous evaporites into contact with the water table, or to surface (Fig. 11), and that this scenario,
736 coupled with diapiric exposures of evaporitic sediments in the proximal basin (Trudgill, 2011; Venus
737 *et al.,* 2015), may have contributed to the recycling of the isotopic signature. At present however, the
738 authors have no direct geological evidence to support this hypothesis.

739 **Implications for using $\Delta^{17}O$ as a palaeoatmospheric proxy in non-marine evaporites**

740 The presence of a dominant late Carboniferous to early Permian marine $\delta^{34}S$ signal in the gypsum
741 deposits analysed here, coupled with the sedimentological constraints precluding marine influence,
742 suggests that the sulphate incorporated into Cedar Mesa was recycled from an older marine evaporite

743 succession. This is entirely reasonable given that the global fluvial sulphate flux is known to be derived
744 from pyrite oxidation and dissolution of calcium sulphate minerals (Halevy *et al.,* 2012; Wortmann &
745 Paytan., 2012). The geology of the hinterland exerts a strong influence on the isotopic composition of
746 fluvial sulphate (Burke *et al.,* 2018; Waldbeck *et al.,* 2019). Given that the Paradox Formation may
747 have been uplifted and possibly even exposed in the footwalls of faults during the Permian Period
748 (Kelley, 1955; Huntoon, 1993; Davis, 1999; Mynatt *et al.,* 2009; Hilley *et al.,* 2010; Pettigrew *et al.,*
749 2019), it seems probable that the hinterland and local area contained a significant proportion of late
750 Carboniferous evaporites. The dissolution of these evaporites, and their incorporation into short-lived,
751 short-distance (tens of kilometres) fluvial systems in the Paradox Basin, may have led to a fluvial
752 sulphate flux that was dominated by sulphate recycled from older evaporite deposits.

753 However, $\delta^{34}S$ and $\Delta^{17}O$ values in the Cedar Mesa Sandstone may not only record recycling of older
754 evaporite signals. Contemporaneous sulphide oxidation in other areas of the drainage basin may also
755 have delivered sulphate to the depositional environments via fluvial systems. It might be expected that
756 this sulphate flux would have a less positive (fluvial) $\delta^{34}S$ value (Burke *et al.,* 2018) and a more negative
757 $\Delta^{17}O$ value (Waldbeck *et al.,* 2019), producing coupled $\delta^{34}S$ and $\Delta^{17}O$ trends; however, with the
758 exception of the lowermost portion of Log 1.4, this is not evident. Additionally, $\delta^{34}S$ values in the Cedar
759 Mesa Sandstone are consistent with late Carboniferous–early Permian seawater $\delta^{34}S$ values. If anything,
760 the average $\delta^{34}S$ value in the Cedar Mesa Sandstone (+14.0‰) is marginally higher than the known
761 Paradox Formation value (+13.3‰; Claypool *et al.,* 1980). It is likely that significant mixing of a
762 sulphide oxidation flux into the fluvial sulphate would have lowered the bulk-rock $\delta^{34}S$ value.
763 Therefore, this process is considered to be a fairly insignificant sulphate source in comparison to the
764 recycling of older marine evaporites. This is in line with other studies that have found limited evidence
765 for alteration of evaporite-derived bulk rock $\delta^{34}S$ values by oxidative sulphide weathering in this study
766 area (Breit *et al.,* 1990).

767 The findings of this study hold very important implications for the interpretation of $\Delta^{17}O$ in continental
768 sulphates, as they too must also have been recycled. As discussed above, continental evaporites could
769 represent a better target for studies attempting to reconstruct coupled biosphere–atmosphere interaction

using $\Delta^{17}O$ as the sulphate in such depositional settings would be: (i) closer to the site of initial sulphide oxidation; and (ii) subjected to less microbial sulphur cycling as is common in the marine realm (i.e. gradual erasure of bulk rock $\Delta^{17}O$ anomalies by oxygen isotope exchange with water). In this regard, continental sulphates hold important potential as terrestrial analogues for sulphate evaporites in extraterrestrial arid environments. In such settings, the erasure/absence of $\Delta^{17}O$ anomalies predicted by abiogenic processes may constitute an unexplored indicator of sulphur cycling by micro-organisms.

This work has shown that, in environments where there is no evidence of marine influence (and sedimentological evidence against it) and where a high proportion of fluvial sulphate is thought to be derived from Ca-sulphate dissolution, the age of the sulphate complex may significantly pre-date the age of the deposit. In the case of the Paradox Formation and the Cedar Mesa Sandstone Formation the depositional age difference may be of the order of 20 to 30 Myr, spanning the Carboniferous–Permian boundary, but for other continental evaporite successions such a time gap may be longer. If the interpretations herein are correct, future studies of the Paradox Formation should reveal significant negative $\Delta^{17}O$ values.

Therefore, in terms of temporal $\Delta^{17}O$ evolution, $\Delta^{17}O$ values in the Cedar Mesa Sandstone Formation may more accurately reflect the atmosphere of the late Carboniferous Period. Even fewer $\Delta^{17}O$ values are known from the Carboniferous Period (n = 13); mid to late Pennsylvanian $\Delta^{17}O$ values range from 0 to -0.15‰ (Bao, 2005; Bao *et al.*, 2008). Hence, the dataset presented here provides an important new constraint on late Carboniferous $\Delta^{17}O$ values.

CONCLUSIONS

By using the Cedar Mesa Sandstone Formation of the Paradox Basin as a case study, this work has demonstrated that evaporites within a transitional setting between desert ergs and saline lakes exhibit unique sedimentological characteristics. The relationships may be summarized by separate models of erg-margin and lacustrine-margin systems. Erg-margin systems represent small-scale saline interdunes

795 hosted between and around dominantly aeolian sediments. Lacustrine-margin systems represent
796 evaporitic development in saline pan and mud flats around an arid saline lake. These settings develop
797 in response to the dominance of either an aeolian erg-margin setting or a lacustrine dominant lake-
798 margin setting due to climatic fluctuations between arid and humid conditions.

799 Sulphur isotope systematics, coupled with detailed sedimentological constraint on depositional
800 processes, shows that marine isotopic signals recorded within gypsum/anhydrite deposits are recycled
801 from older, underlying marine evaporites. This implies that the $\Delta^{17}O$ 'atmospheric fingerprint' within
802 these early Permian non-marine deposits does not date to the time of deposition. Rather, the $\Delta^{17}O$ values
803 reflect late Pennsylvanian atmospheric conditions; older $\Delta^{17}O$ values have been recycled into younger
804 evaporites. Therefore, in dryland settings, the heightened potential for sulphate weathering and
805 reprecipitation, raises the possibility that the age of a sulphate complex and the age of the host evaporite
806 deposit could be decoupled from one another. This holds important implications for studies attempting
807 to reconstruct temporal $\Delta^{17}O$ trends from non-marine evaporites.

808 There are, to the authors' knowledge, no $\Delta^{17}O$ values published from either the late Carboniferous or
809 early Permian periods. Therefore, provided the temporal caveats outlined above are applied, the $\Delta^{17}O$
810 data presented here can be used to constrain coupled biosphere–atmosphere evolution during the
811 Phanerozoic Eon. They can be included in $\Delta^{17}O$ compilations because the source of the recycled signals
812 has been constrained. This, however, may not be the case for all non-marine evaporites.

813 To avoid misleading interpretations of secular $\Delta^{17}O$ change, isotopic data must be closely integrated
814 with sedimentological processes, basin evolution, regional geology and evaporite paragenesis. Such
815 contextual work should be conducted in future $\Delta^{17}O$ studies targeting non-marine evaporites so that the
816 temporal fidelity of $\Delta^{17}O$ signals can be verified.

817 # ACKNOWLEDGMENTS

818 This research was supported by grants to RPP from the AAPG (Gustavus E. Archie Memorial Grant)
819 and by the European Union's Horizon 2020 research and innovation programme (Grant 678812 to

M.W.C.). The authors thank The U.S. National Park Service, the Rangers of Canyonlands National Park and the Navajo Nation for permitting field-based data collection. Kathleen Benison, Steven Banham and Bernard Besly are thanked for their constructive comments and reviews of earlier versions of this manuscript. Andrew Mitten and David Cousins are thanked for assistance in the field. We thank Yongbo Peng and Huiming Bao at the OASIC laboratory (Louisiana State University) for their assistance in measuring oxygen isotopes. The authors declare that they have no conflict of interests.

DATA AVAILABILITY STATEMENT

The data that support the findings of this study are available from the corresponding author upon reasonable request.

REFERENCES

Aerts, J.W., van Spanning, R.J., Flahaut, J., Molenaar, D., Bland, P.A., Genge, M.J., Ehrenfreund, P. and **Martins, Z.,** (2019). Microbial Communities in Sediments From Four Mildly Acidic Ephemeral Salt Lakes in the Yilgarn Craton (Australia)–Terrestrial Analogs to Ancient Mars. *Frontiers in microbiology*, ***10***, p.779.

Abrantes Jr, F.R., Nogueira, A.C. and **Soares, J.L**. (2016) Permian paleogeography of west-central Pangea: Reconstruction using sabkha-type gypsum-bearing deposits of Parnaíba Basin, Northern Brazil. *Sedimentary Geology*, **341**.175-188.

Ahlbrandt, T.S. and **Fryberger, S.G**. (1981) Sedimentary features and significance of interdune deposits. In: *Recent and Ancient Nonmarine Depositional Environments: Models for Exploration* (Eds F.G. Ethridge and R.M. Flores) *SEPM Spec. Publ.*, **31**, 293-314.

Alderman, S.S. (1985) Geology of the Owens Lake evaporite deposit. In: *Sixth international symposium on salt* (Eds B. C. Schreiber and H. L. Harner) *Alexandria: Salt Institute.* 1, 75-83.

842 **Al-Masrahy, M. A**., and **Mountney, N. P**. (2015). A classification scheme for fluvial–aeolian system
843 interaction in desert-margin settings. *Aeolian Research*, **17**, 67-88.

844 **Anderson, R. Y., Allen, B. D.,** and **Menking, K. M.** (2002). Geomorphic expression of abrupt climate
845 change in southwestern North America at the glacial termination. *Quaternary Research*, **57**(3), 371-
846 381.

847 **Antrett, P**. (2013). Characterization of an Upper Permian Tight Gas Reservoir: A Multidisciplinary,
848 Multiscale Analysis from the Rotliegend, Northern Germany. Springer Science & Business Media.

849 **Baars, D.L.,** (1962) Permian system of Colorado Plateau. *AAPG Bulletin*, **46,** 149-218.

850 **Baars, D.L.,** (1979) The Permian System. In: *Permianland* (Ed. D.L. Baars). *Four Corners Geological*
851 *Society, 9th Field Conference Guidebook* pp 1-6

852 **Baker, A. A.** (1946). Geology of the Green River Desert-cataract Canyon Region: Emery, Wayne, and
853 Garfield Counties, Utah (No. 950-952). *US Government Printing Office*.

854 **Balci, N., Shanks III, W. C., Mayer, B**., and **Mandernack, K. W**. (2007). Oxygen and sulfur isotope
855 systematics of sulfate produced by bacterial and abiotic oxidation of pyrite. *Geochimica et*
856 *Cosmochimica Acta*, **71**(15), 3796-3811.

857 **Banham, S. G.,** and **Mountney, N. P**. (2013). Evolution of fluvial systems in salt-walled mini-basins:
858 a review and new insights. *Sedimentary Geology*, **296**, 142-166.

859 **Bao, H**. (2005). Sulfate in modern playa settings and in ash beds in hyperarid deserts: implication for
860 the origin of 17O-anomalous sulfate in an Oligocene ash bed. *Chemical geology*, ***214***(1-2), 127-134.

861 **Bao, H**., (2006) Purifying barite for oxygen isotope measurement by dissolution and reprecipitation in
862 a chelating solution. *Analytical chemistry*, **78**, 304-309.

863 **Bao, H**. (2015). Sulfate: a time capsule for Earth's O2, O3, and H2O. *Chemical Geology*, ***395***, 108-118.

Bao, H., Lyons, J.R. and **Zhou, C.,** (2008). Triple oxygen isotope evidence for elevated CO 2 levels after a Neoproterozoic glaciation. *Nature*, ***453***(7194), pp.504-506.

Barbeau, D.L. (2003) A flexural model for the Paradox Basin: implications for the tectonics of the Ancestral Rocky Mountains. *Basin Research*, **15**, 97-15.

Benison, K. C. (2006). A martian analog in Kansas: comparing martian strata with Permian acid saline lake deposits. *Geology*, **34**, 385-388.

Benison, K. C. and **Goldstein, R. H**. (2000). Sedimentology of ancient saline pans: an example from the Permian Opeche Shale, Williston Basin, North Dakota, USA. *Journal of Sedimentary Research*, **70**, 159-169.

Benison, K.C. and **Bowen, B.B**., (2013) Extreme sulfur-cycling in acid brine lake environments of Western Australia. Chemical Geology, 351, pp.154-167.

Benison, K.C. and **Bowen, B.B**., (2006) Acid saline lake systems give clues about past environments and the search for life on Mars. *Icarus*, **183**, 225-229.

Benison, K.C. and **Goldstein, R.H.** (2001) Evaporites and siliciclastics of the Permian Nippewalla Group of Kansas, USA: a case for non-marine deposition in saline lakes and saline pans. *Sedimentology*, **48**, 165-188.

Benison, K.C. and **Goldstein, R.H**., (1999) Permian paleoclimate data from fluid inclusions in halite. *Chemical Geology*, **154**, 113-132.

Benison, K.C., Bowen, B.B., Oboh-Ikuenobe, F.E., Jagniecki, E.A., LaClair, D.A., Story, S.L., Mormile, M.R. and **Hong, B.Y**., (2007). Sedimentology of acid saline lakes in southern Western Australia: newly described processes and products of an extreme environment. *Journal of Sedimentary Research*, ***77***(5), pp.366-388.

Benison, K.C., Zambito IV, J.J. and **Knapp, J**., (2015) Contrasting siliciclastic–evaporite strata in subsurface and outcrop: an example from the Permian Nippewalla Group of Kansas, USA. *Journal of Sedimentary Research*, 85(6), pp.626-645.

Biswas, A. (2005) Coarse aeolianites: sand sheets and zibar–interzibar facies from the Mesoproterozoic Cuddapah Basin, India. *Sedimentary Geology*, **174**, 149-160Blair & McPherson, 1994;

Blakey, R.C., (1988) Basin tectonics and erg response. *Sedimentary Geology*, **56**, 127–151.

Blakey, R.C., (1996) Permian eolian deposits, sequences and sequence boundaries, Colorado Plateau. In: *Paleozoic Systems of the Rocky Mountain Region* (Eds M.W. Longman and S.D. Sonnenfeld), *Rocky Mountain Section SEPM*, 405–426.

Blakey, R.C., Peterson, F. and **Kocurek, G.** (1988) Synthesis of late Paleozoic and Mesozoic eolian deposits of the Western Interior of the United States. *Sedimentary Geology*, **56**, 3-125.

Blamey, N.J., Brand, U., Parnell, J., Spear, N., Lécuyer, C., Benison, K., Meng, F. and **Ni, P.,** (2016). Paradigm shift in determining Neoproterozoic atmospheric oxygen. *Geology*, **44**(8), pp.651-654.

Blättler, C.L., Claire, M.W., Prave, A.R., Kirsimäe, K., Higgins, J.A., Medvedev, P.V., Romashkin, A.E., Rychanchik, D.V., Zerkle, A.L., Paiste, K. and **Kreitsmann, T.,** (2018). Two-billion-year-old evaporites capture Earth's great oxidation. *Science*, 360(6386),.320-323.

Blissenbach, E. (1954). Geology of alluvial fans in semiarid regions. *Geological Society of America Bulletin*, ***65***, 175-190.

Boehrer, B. and **Schultze, M.** (2008). Stratification of lakes. *Reviews of Geophysics*, **46**, 1-27.

Boggs Jr, S., and **Boggs, S**. (2009). *Petrology of sedimentary rocks*. Cambridge university press.

Breit, George N., Martin B. Goldhaber, Daniel R. Shawe, and **E. Craig Simmons**. (1990) Authigenic barite as an indicator of fluid movement through sandstones within the Colorado Plateau. *Journal of Sedimentary Research* 60, **6**: 884-896.

910 **Bridge, J. S**., and **R. V. Demicco**, (2008), Earth surface processes, landforms and sediment deposits:
911 New York, Cambridge University Press, 830 p.

912 **Bridge, J.S.** (1993) The interaction between channel geometry, water flow, sediment transport and
913 deposition in braided rivers. In: *Braided Rivers* (eds J. L. Best & C. S. Bristow), *Spec. Publishers Geol.*
914 *Soc. Lond.*, 75, 13–71.

915 **Brooks, R. A**., and **Ferrell Jr, R. E**. (1970). The lateral distribution of clay minerals in Lakes
916 Pontchartrain and Maurepas, Louisiana. *Journal of Sedimentary Research*, **40**.

917 **Bull, W. B.** (1977). The alluvial-fan environment. *Progress in Physical geography*, **1**, 222-270.

918 **Butler, G. P**. (1970). Secondary anhydrite from a sabkha, northwest Gulf of California, Mexico.
919 In *Third symposium on salt* (Vol. **1**, pp. 153-155). Northern Ohio geol. Soc..

920 **Cain, S.A.** and **Mountney, N.P.** (2009) Spatial and temporal evolution of a terminal fluvial fan system:
921 the Permian Organ Rock Formation, South-east Utah, USA. *Sedimentology*, **56**, 1774-1800.

922 **Cao, X.,** and **Bao, H.** (2013). Dynamic model constraints on oxygen-17 depletion in atmospheric O2
923 after a snowball Earth. Proceedings of the National Academy of Sciences, **110**(36), 14546-14550.

924 **Carter, D.C.** and **Pickerill, R.K.,** (1985). Algal swamp, marginal and shallow evaporitic lacustrine
925 lithofacies from the Late Devonian-Early Carboniferous Albert Formation, southeastern New
926 Brunswick, Canada. *Atlantic Geology* **21** 69-86

927 **Casas, E.,** and **Lowenstein, T. K.** (1989). Diagenesis of saline pan halite; comparison of petrographic
928 features of modern, Quaternary and Permian halites. *Journal of sedimentary Research*, **59**(5), 724-739.

929 **Castens-Seidell, B.** (1984) Morphologies of Gypsum on a Modern Sabkha: Clues to Depositional
930 Conditions. *AAPG Bulletin*, **68**, 460-460.

931 **Cecil, C.B.** (1990) Paleoclimate controls on stratigraphic repetition of chemical and siliciclastic rocks.
932 *Geology*, **18**, 533-536.

Chiba, H., Kusakabe, M., Hirano, S. I., Matsuo, S., & **Somiya, S**. (1981). Oxygen isotope fractionation factors between anhydrite and water from 100 to 550 C. *Earth and Planetary Science Letters*, **53**(1), 55-62.

Claypool, G.E., Holser, W.T., Kaplan, I.R., Sakai, H. and **Zak, I.** (1980) The age curves of sulfur and oxygen isotopes in marine sulfate and their mutual interpretation. *Chemical Geology*, **28**, 199-260

Condon, S.M. (1997) Geology of the Pennsylvanian and Permian Cutler Group and Permian Kaibab Limestone in the Paradox Basin, Southeastern Utah and Southwestern Colorado. *US Geol. Surv. Bull.*, **2000-P**, 46 pp

Crockford, P.W., Cowie, B.R., Johnston, D.T., Hoffman, P.F., Sugiyama, I., Pellerin, A., Bui, T.H., Hayles, J., Halverson, G.P., Macdonald, F.A. and **Wing, B.A**., (2016). Triple oxygen and multiple sulfur isotope constraints on the evolution of the post-Marinoan sulfur cycle. *Earth and Planetary Science Letters*, 435, pp.74-83.

Crockford, P.W., Hayles, J.A., Bao, H., Planavsky, N.J., Bekker, A., Fralick, P.W., Halverson, G.P., Bui, T.H., Peng, Y. and **Wing, B.A.,** (2018). Triple oxygen isotope evidence for limited mid-Proterozoic primary productivity. *Nature*, 559(7715), pp.613-616.

Crockford, P.W., Kunzmann, M., Bekker, A., Hayles, J., Bao, H., Halverson, G.P., Peng, Y., Bui, T.H., Cox, G.M., Gibson, T.M. and **Wörndle, S.,** (2019). Claypool continued: Extending the isotopic record of sedimentary sulfate. *Chemical Geology*.

Denison, R. E., Kirkland, D. W., & **Evans, R.** (1998). Using strontium isotopes to determine the age and origin of gypsum and anhydrite beds. *The journal of Geology*, ***106***(1), 1-18.

Dickinson, W.R., Soreghan, G.S. and **Giles, K.A.** (1994) Glacio-eustatic origin of Permo-Carboniferous stratigraphic cycles; evidence from the southern Cordilleran foreland region. In: *Tectonic and Eustatic Controls on Sedimentary Cycles* (Eds. J.M. Dennison & F.R. Ettensohn), *SEPM,* 25–34 pp

957 **Dickinson, W. R.,** and **Gehrels, G. E**. (2003). U–Pb ages of detrital zircons from Permian and Jurassic
958 eolian sandstones of the Colorado Plateau, USA: paleogeographic implications. *Sedimentary*
959 *Geology*, **163**(1-2), 29-66.

960 **Doe, T.W.** and **Dott, R.H.** (1980) Genetic significance of deformed cross bedding; with examples from
961 the Navajo and Weber sandstones of Utah. *Journal of Sedimentary Research*, **50**, 793-812

962 **dos Reis, A.D., dos Santos Scherer, C.M., do Amarante, F.B., Rossetti, M.D.M.M., Kifumbi, C.,**
963 **de Souza, E.G., Ferronatto, J.P.F**. and **Owen, A.,** (2019). Sedimentology of the proximal portion of
964 a large-scale, Upper Jurassic fluvial-aeolian system in Paraná Basin, southwestern Gondwana. Journal
965 of South American Earth Sciences, 95, p.102248.

966 **Driese, S. G.** (1985). Interdune pond carbonates, Weber Sandstone (Pennsylvanian-Permian), northern
967 Utah and Colorado. *Journal of Sedimentary Research*, ***55***, 187-195.

968 **Dubiel, R.F., Huntoon, J.E., Condon, S.M.** and **Stanesco, J.D.** (1996) Permian deposystems,
969 paleogeography, and paleoclimate of the Paradox basin and vicinity. In: *Paleozoic Systems of the Rocky*
970 *Mountain Region* (Eds M.W. Longman and S.D. Sonnenfeld), *Rocky Mountain Section SEPM*, 405–
971 426.

972 **Eberth, D.A.** and **Miall, A.D.** (1991) Stratigraphy, sedimentology and evolution of a vertebrate-
973 bearing, braided to anastomosed fluvial system, Cutler Formation (Permian-Pennsylvanian), north-
974 central New Mexico. *Sedimentary Geology*, **72**, 225-252.

975 **Falcon-Lang, H.J., Lucas, S.G., Kerp, H., Krainer, K., Montañez, I.P., Vachard, D., Chaney, D.S.,**
976 **Elrick, S.D., Contreras, D.L., Kurzawe, F.** and **DiMichele, W.A**., (2015). Early Permian (Asselian)
977 vegetation from a seasonally dry coast in western equatorial Pangea: Paleoecology and evolutionary
978 significance. *Palaeogeography, Palaeoclimatology, Palaeoecology*, *433*, pp.158-173.

979 **Fenton L.K. Bishop J.L. Lafuente B. Horgan B.H. Szynkiewicz A. Bustos D**. and **King S.J.** (2014)
980 Preliminary results from a field study of the mineralogy of White Sands National Monument Dune
981 Field. *Lunar and Planetary Science Conference XLV*, The Woodlands, Texas, Abstract 2855.

Ferronatto, J. P. F., dos Santos Scherer, C. M., de Souza, E. G., dos Reis, A. D., and **de Mello, R**. G. (2019). Genetic units and facies architecture of a Lower Cretaceous fluvial-aeolian succession, São Sebastião Formation, Jatobá Basin, Brazil. *Journal of South American Earth Sciences*, 89, 158-172.

Fielding, C.R. (1984) Upper delta plain lacustrine and fluviolacustrine facies from the Westphalian of the Durham coalfield, NE England. *Sedimentology*, **31**, 547-567.

Fischer, A. G., & **Roberts, L. T.** (1991). Cyclicity in the Green River formation (lacustrine Eocene) of Wyoming. *Journal of Sedimentary Research*, *61*(7), 1146-1154

Fishbaugh, K. E., Poulet, F., Chevrier, V., Langevin, Y., & **Bibring, J. P**. (2007). On the origin of gypsum in the Mars north polar region. *Journal of Geophysical Research: Planets*, **112**(E7).

Flügel, E. (2004) Depositional Models, Facies Zones and Standard Microfacies. In: *Microfacies of Carbonate Rocks* (Ed E. Flügel) 2nd edn, pp. 657-724. Springer, Berlin.

Foster, T. M., Soreghan, G. S., Soreghan, M. J., Benison, K. C., & **Elmore, R. D.** (2014). Climatic and paleogeographic significance of eolian sediment in the Middle Permian Dog Creek Shale (Midcontinent US). *Palaeogeography, Palaeoclimatology, Palaeoecology*, ***402***, 12-29.

Gay R.J., Huttenlocker A.K., Irmis R.B., Stegner M.A., and **Uglesich J.,** (2020), Paleontology of Bears Ears National Monument (Utah, USA): History of exploration, study, and designation : *Geology of the Intermountain West*, **7**, 205-241.

Glennie, K.W. (1972) Permian Rotliegendes of northwest Europe interpreted in light of modern desert sedimentation studies. *AAPG Bulletin*, **56**, 1048-1071.

Goldstein, R.H. and **Reynolds T.J.** (1994) Systematics of Fluid Inclusions in Diagenetic Minerals, SEMP (Society of Sedimentary Geology) Short Course, vol. 31.199 pp.

Goodall, T. M., North, C. P., and **Glennie, K. W**. (2000). Surface and subsurface sedimentary structures produced by salt crusts. *Sedimentology*, ***47***, 99-118.

Gündogan, I., Önal, M., and **Depçi, T.** (2005). Sedimentology, petrography and diagenesis of Eocene–Oligocene evaporites: the Tuzhisar Formation, SW Sivas Basin, Turkey. Journal of Asian Earth Sciences, **25**, 791-803.

Halevy, I., Peters, S. E., and **Fischer, W. W**. (2012). Sulfate burial constraints on the Phanerozoic sulfur cycle. *Science*, **337**(6092), 331-334.

Handford, C. R. (1991) Marginal Marine Halite: Sabkhas and Salinas. In *Developments in sedimentology* (Vol. **50**, pp. 1-66). Elsevier.

Hardie, L.A., Lowenstein, T.K. and **Spencer, R.J.** (1985) The problem of distinguishing between primary and secondary features in evaporites. In *Sixth international symposium on salt* (Eds B. C. Schreiber and H. L. Harner) *Alexandria: Salt Institute.* 1, 11-39.

Harvey, A. M., Mather, A. E., and **Stokes, M.** (2005). Alluvial fans: geomorphology, sedimentology, dynamics—introduction. In: *A review of alluvial-fan research.* (Eds: Harvey, A. M., Mather, A. E., and Stokes, M) *Geological Society, London, Special Publications,* **251**, 1-7.

Helvaci, C. (1995). Stratigraphy, mineralogy, and genesis of the Bigadiç borate deposits, Western Turkey. *Economic Geology*, *90*(5), 1237-1260.

Hemingway, J.D., Olson, H., Turchyn, A.V., Tipper, E.T., Bickle, M.J. and **Johnston, D.T.,** (2020). Triple oxygen isotope insight into terrestrial pyrite oxidation. *Proceedings of the National Academy of Sciences*, *117*(14), pp.7650-7657.

Herries, R.D. (1993) Contrasting styles of fluvial-aeolian interaction at a downwind erg margin: Jurassic Kayenta-Navajo transition, northeastern Arizona, USA. In: *Characterization of Fluvial and Aeolian Reservoirs* (Eds C.P. North and D. J. Prosser) *Geological Society, London, Special Publications,* 73, 199-218.

Hooke, R. L. (1967). Processes on arid-region alluvial fans. *The Journal of Geology*, **75**, 438-460.

Horita, J., Zimmermann, H., and **Holland, H. D**. (2002). Chemical evolution of seawater during the Phanerozoic: Implications from the record of marine evaporites. *Geochimica et Cosmochimica Acta*, *66*(21), 3733-3756.

Horowitz, D.H. (1982) Geometry and origin of large-scale deformation structures in some ancient wind-blown sand deposits. *Sedimentology*, **29**, 155-180.

Howell, J. and **Mountney, N.** (1997) Climatic cyclicity and accommodation space in arid to semi-arid depositional systems: an example from the Rotliegend Group of the UK southern North Sea. In: *Petroleum Geology of the Southern North Sea: Future Potential* (Eds K. Ziegler, P. Turner and S. R. Daines) *Geological Society, London, Special Publications*, **123**, 63-86.

Hudson, J.D. (1977) Stable isotopes and limestone lithification. *Journal of the Geological Society*, **133**, 637-660.

Huerta, P., Armenteros, I., Recio, C. and **Blanco, J.A.,** (2010). Palaeogroundwater evolution in playa–lake environments: sedimentary facies and stable isotope record (Palaeogene, Almazán Basin, Spain). Palaeogeography, Palaeoclimatology, Palaeoecology, **286**(3-4), pp.135-148.

Huntoon, J.E., Dubiel, R.F., Stanesco, J.D., Mickelson, D. and **Condon, S.M.** (1996) Permian-Triassic depositional systems, paleogeography, paleoclimate, and hydrocarbon resources in Canyonlands and Monument Valley, Utah. *Geological Society of America Fieldguide*, **3**, 26 pp.

Huntoon, J.E., Stanesco, J.D., Dubiel, R.F. and **Dougan, J.** (2000) Geology of Natural Bridges National Monument, Utah. In: Geology of Utah's Parks and Monuments (Eds D.A. Sprinkel, T.C. Chidsey and P.B. Anderson), Utah Geol. Assoc. Publ., **28**, 233–249.

Johnson, S.S., Chevrette, M.G., Ehlmann, B.L. and **Benison, K.C**., (2015). Insights from the metagenome of an acid salt lake: the role of biology in an extreme depositional environment. *PLoS One*, *10*(4), p.e0122869.

Jordan, O.D. and **Mountney, N.P.** (2010) Styles of interaction between aeolian, fluvial and shallow marine environments in the Pennsylvanian to Permian lower Cutler beds, south-east Utah, USA. *Sedimentology*, **57**, 1357-1385.

Jordan, O.D. and **Mountney, N.P.** (2012) Sequence stratigraphic evolution and cyclicity of an ancient coastal desert system: the Pennsylvanian–Permian Lower Cutler Beds, Paradox Basin, Utah, USA. *Journal of Sedimentary Research*, **82**, 755-780.

Kampschulte, A., and **Strauss, H**. (2004). The sulfur isotopic evolution of Phanerozoic seawater based on the analysis of structurally substituted sulfate in carbonates. *Chemical Geology*, *204*(3-4), 255-286.

Kendall, A.C. (1978) Facies models 11. Continental and supratidal (sabkha) evaporites. *Geoscience Canada*, **5,** 66-78.

Kendall, A.C. (1981) Continental and supratidal (sabkha) evaporates. In: *Facies Models*, (Ed. Walker, R.G.), *Geoscience Canada*, 145-157

Kendall, A.C., and **Harwood, G.M.,** (1996) Marine evaporites: arid shorelines and basins. In: Sedimentary environments: Processes, facies and stratigraphy (ed. H.G. Reading): 281-324. Blackwell Science.

Kessler, J. L., Soreghan, G. S., and **Wacker, H. J.** (2001). Equatorial aridity in western Pangea: Lower Permian loessite and dolomitic paleosols in northeastern New Mexico, USA. *Journal of Sedimentary Research*, ***71*(5)**, 817-832.

Killingsworth, B. A., Bao, H., and **Kohl, I. E**. (2018). Assessing pyrite-derived sulfate in the Mississippi River with four years of sulfur and triple-oxygen isotope data. Environmental science & technology, 52(11), 6126-6136.

Kocurek, G. (1996) Deserts Aeolian systems. In *Sedimentary environments: processes, facies and stratigraphy* (Ed. H.G. Reading) 3rd edn, pp. 125-153. Blackwell Science, Oxford

Kocurek, G., (1981) Significance of interdune deposits and bounding surfaces in aeolian dune sands. *Sedimentology*, **28**, 753-780

Kocurek, G., (1991) Interpretation of ancient eolian sand dunes. *Annual Review of Earth and Planetary Sciences*, **19**, 43-75

Kocurek, G., and **Nielson, J.** (1986) Conditions favourable for the formation of warm-climate aeolian sand sheets. *Sedimentology*, **33**, 795-816.

Kocurek, G., Carr, M., Ewing, R., Havholm, K. G., Nagar, Y. C., & **Singhvi, A. K**. (2007). White Sands Dune Field, New Mexico: age, dune dynamics and recent accumulations. *Sedimentary Geology*, ***197***(3-4), 313-331.

Kohl, I., and **Bao, H**. (2011). Triple-oxygen-isotope determination of molecular oxygen incorporation in sulfate produced during abiotic pyrite oxidation (pH= 2–11). Geochimica et Cosmochimica Acta, **75**(7), 1785-1798.

Kovalevich, V. M. (1975). Thermometric studies of inclusions in artificial crystals of halite. *Fluid Inclusion Research*, *8*, 96.

Kusakabe, M., and **Robinson, B. W.** (1977). Oxygen and sulfur isotope equilibria in the BaSO4□ HSO4−□ H2O system from 110 to 350° C and applications. *Geochimica et Cosmochimica Acta*, *41*(8), 1033-1040.

Langevin, Y., Poulet, F., Bibring, J. P., and **Gondet, B.** (2005). Sulfates in the north polar region of Mars detected by OMEGA/Mars Express. *Science*, *307*(5715), 1584-1586.

Langford, R. P. (2003). The Holocene history of the White Sands dune field and influences on eolian deflation and playa lakes. *Quaternary International*, ***104***(1), 31-39.

Langford, R.P. (1989). Fluvial-aeolian interactions: Part I, modern systems. *Sedimentology*, **36**, 1023-1035.

Langford, R.P. and **Chan, M.A.,** (1989) Fluvial-aeolian interactions: Part II, ancient systems. *Sedimentology*, **36**, 1037-1051

Langford, R.P. and **Chan, M.A.,** (1993) Downwind changes within an ancient dune sea, Permian Cedar Mesa Sandstone, southeast Utah. In: *Aeolian Sediments: Ancient and Modern* (Eds K. Pye and N. Lancaster), pp. 109–126. Blackwell Publishing Ltd., Oxford, UK.

Langford, R.P. and **Massad, A**. (2014) Facies geometries and climatic influence on stratigraphy in the eolian-sabkha transition in the Permian Cedar Mesa Sandstone, SE Utah In: *Geology of Utah's Far South,* (Eds J.S.MacLean, R.F. Biek, and J.E. Huntoon) *Utah Geological Association Publication*, **43**, 275-294.

Last, W.M. (1984) Sedimentology of playa lakes of the northern Great Plains. *Canadian Journal of Earth Sciences*, **21**, 107-125.

Lawton, T. F., and **Buck, B. J.** (2006). Implications of diapir-derived detritus and gypsic paleosols in Lower Triassic strata near the Castle Valley salt wall, Paradox Basin, Utah. *Geology*, **34**(10), 885-888.

Lockley, M. G., and **Madsen Jr, J. H.** (1993). Early Permian vertebrate trackways from the Cedar Mesa sandstone of eastern Utah: Evidence of predator-prey interaction. *Ichnos: An International Journal of Plant & Animal*, ***2*****(**2), 147-153.

Lokier, S. and **Steuber, T.** (2008) Quantification of carbonate-ramp sedimentation and progradation rates for the late Holocene Abu Dhabi shoreline. *Journal of Sedimentary Research*, **78**, 423-431.

Lokier, S. and **Steuber, T.** (2009) Large-scale intertidal polygonal features of the Abu Dhabi coastline. *Sedimentology*, **56**, 609-621.

Loope, D.B. (1981) Deposition, Deflation and Diagenesis of Upper Paleozoic Eolian Sediments, Canyonlands National Park, Utah. Unpublished PhD Thesis, University of Wyoming, Laramie, 170 pp

Loope, D.B. (1984) Eolian origin of upper Paleozoic sandstones, southeastern Utah. *Journal of Sedimentary Research*, **54**, 563-580.

Lowenstein, T. K., and **Spencer, R. J.** (1990). Syndepositional origin of potash evaporites; petrographic and fluid inclusion evidence. *American Journal of Science*, *290*(1), 1-42.

Lowenstein, T. K., Timofeeff, M. N., Kovalevych, V. M., and **Horita, J.** (2005). The major-ion composition of Permian seawater. *Geochimica et Cosmochimica Acta*, ***69***(7), 1701-1719.

Lowenstein, T.K. and **Hardie, L.A.** (1985) Criteria for the recognition of salt-pan evaporites. *Sedimentology*, **32**, 627-644.

Lucas, S.G., and **Krainer, K**. (2005) Cutler Group (Permo-Carboniferous) stratigraphy, Chama basin, New Mexico. In: *The Permian of Central New Mexico*, (Eds. S.G. Lucas, K.E. Zeigler, J.A. Spielmann) New Mexico Museum of Natural History and Science Bull., vol. 31, pp. 90-100

Mack, G.H. (1977) Depositional environments of the Cutler-Cedar Mesa facies transition (Permian) near Moab, Utah. *The Mountain Geologist*, **14**, 53-68

Mack, G.H. (1979) Littoral marine depositional model for the Cedar Mesa Sandstone (Permian), Canyonlands National Park, Utah. In: Permianland (Ed. D.L. Baars). *Four Corners Geological Society, 9th Field Conference Guidebook*. pp. 33–37

Martel, A.T. and **Gibling, M.R.** (1991) Wave-dominated lacustrine facies and tectonically controlled cyclicity in the Lower Carboniferous Horton Bluff Formation, Nova Scotia, Canada. In: *Lacustrine facies analysis* (Eds. P. Anadon, L. Cabera and K. Kelts) *International Association of Sedimentologists, Special Publication* **13**, 223-243.

Martin, J.H. and **Evans, P.F.** (1988). Reservoir modeling of marginal aeolian/sabkha sequences, Southern North Sea (UK sector). Society of Petroleum Engineers, Houston, Texas, 63rd Annual Technical Conference and Exhibition, October 2–5, **SPE 18155**, p. 473–486.

McKee, E.D., Douglass, J.R. and **Rittenhouse, S.** (1971) Deformation of lee-side laminae in eolian dunes. *Geological Society of America Bulletin*, **82**, 359-378.

McKight, E.T., (1940) Geology of area between Green and Colorado rivers, Grand and San Juan counties, Utah. *US Government Printing Office*

Mertz Jr, K. A., and **Hubert, J. F.** (1990). Cycles of sand-flat sandstone and playa–lacustrine mudstone in the Triassic–Jurassic Blomidon redbeds, Fundy rift basin, Nova Scotia: implications for tectonic and climatic controls. *Canadian Journal of Earth Sciences*, ***27***, 442-451

Miall, A. D. (1985). Architectural-element analysis: a new method of facies analysis applied to fluvial deposits. *Earth-Science Reviews*, ***22***, 261-308.

Miall, A.D. (1996) The Geology of Fluvial Deposits: Sedimentary Facies, Basin Analysis and Petroleum Geology. Springer, Berlin, 582 pp.

Mitten, A.J., Howell, L. P., Clarke, S.M. and **Pringle, J.K**., (2020) Controls on the deposition and preservation of architectural elements within a fluvial multi-storey sandbody. *Sedimentary Geology* (**401)**

Mountney, N.P. (2006) Periodic accumulation and destruction of aeolian erg sequences in the Permian Cedar Mesa Sandstone, White Canyon, southern Utah, USA. *Sedimentology*, **53**, 789-823.

Mountney, N.P. and **Jagger, A.** (2004) Stratigraphic evolution of an aeolian erg margin system: the Permian Cedar Mesa Sandstone, SE Utah, USA. *Sedimentology*, **51**, 713-743.

Mountney, N.P. and **Thompson, D.B.** (2002) Stratigraphic evolution and preservation of aeolian dune and damp/wet interdune strata: an example from the Triassic Helsby Sandstone Formation, Cheshire Basin, UK. *Sedimentology*, **49**, 805-833.

North, C. P., and **Davidson, S. K.** (2012). Unconfined alluvial flow processes: recognition and interpretation of their deposits, and the significance for palaeogeographic reconstruction. *Earth-Science Reviews*, *111*(1-2), 199-223.

Nuccio, V.F. and **Condon, S.M.,** (1996) Burial and thermal history of the Paradox Basin, Utah and Colorado, and petroleum potential of the Middle Pennsylvanian Paradox Basin. *US Geol. Surv. Bull.,* **2000-O**, 20 pp

Ortí, F., Rosell, L. and AnadÓN, P., (2003). Deep to shallow lacustrine evaporites in the Libros Gypsum (southern Teruel Basin, Miocene, NE Spain): an occurrence of pelletal gypsum rhythmites. *Sedimentology*, 50(2), pp.361-386.

Ortí, F., Rosell, L., Inglès, M. and **Playa, E.**, (2007). Depositional models of lacustrine evaporites in the SE margin of the Ebro Basin (Paleogene, NE Spain). *Geologica Acta: an international earth science journal*, **5**(1), pp.19-34.

Owen, R.A., Owen, R.B., Renaut, R.W., Scott, J.J., Jones, B. and **Ashley, G.M.** (2008) Mineralogy and origin of rhizoliths on the margins of saline, alkaline Lake Bogoria, Kenya Rift Valley. *Sedimentary Geology*, **203**, 143-163.

Pack, A., Höweling, A., Hezel, D.C., Stefanak, M.T., Beck, A.K., Peters, S.T., Sengupta, S., Herwartz, D. and **Folco, L.,** (2017). Tracing the oxygen isotope composition of the upper Earth's atmosphere using cosmic spherules. *Nature communications*, ***8*(**1).1-7.

Palmer, M. R., Helvací, C., and **Fallick, A. E.** (2004). Sulphur, sulphate oxygen and strontium isotope composition of Cenozoic Turkish evaporites. Chemical Geology, **209**(3-4), 341-356.

Parrish, J. T. (1993). Climate of the supercontinent Pangea. *The Journal of Geology*, *101*(2), 215-233.

Parsons, A. J., and **Abrahams, A. D.** (2009). Geomorphology of desert environments. In Geomorphology of Desert Environments (pp. 3-7). Springer, Dordrecht.

Peng, Y., Bao, H., Zhou, C. and **Yuan, X**., (2011). 17O-depleted barite from two Marinoan cap dolostone sections, South China. *Earth and Planetary Science Letters*, *305*(1-2), pp.21-31.

Peterson, F., (1988) Stratigraphy and nomenclature of middle and upper Jurassic rocks, Western Colorado Plateau, Utah and Arizona. *US Geological Survey*, *Bulletin*, 13-56.

Petrichenko, I.O., (1979), Methods of study of inclusions in minerals of saline deposits:*Fluid Inclusion Research*, v. 12, 214–274.

Pettigrew, R.P., Rogers, S.L., and **Clarke, S.M**. (2019) A microfacies analysis of arid continental carbonates from the Cedar Mesa Sandstone Formation, Utah, USA. *The Depositional Record*. **2020; 6**: 41– 61.

Platt, N.H. and **Wright, V.P.** (1991) Lacustrine carbonates: facies models, facies distributions and hydrocarbon aspects. In: *Lacustrine facies analysis*. (Eds P. Anadon, L. Cabrera and K. Kelts) *Special Publication of the International Association of Sedimentologists*. 13, 57-74

Priddy, C. L., Pringle, J. K., Clarke, S. M., and **Pettigrew, R. P**. (2019). Application of photogrammetry to generate quantitative geobody data in ephemeral fluvial systems. *The Photogrammetric Record*, ***34***(168), 428-444.

Priddy, C., and **Clarke, S. M**. (2020). The sedimentology of an ephemeral fluvial-aeolian succession. *Sedimentology*.

Purvis, K. (1991) Stoss-side mud-drapes: deposits of interdune pond margins. *Sedimentology*, **38**, 153-156

Quigley, M. C., Sandiford, M., and **Cupper, M. L**. (2007). Distinguishing tectonic from climatic controls on range-front sedimentation. *Basin Research*, ***19***, 491-505.

Raab, M. & **Spiro, B.,** (1991). Sulfur isotopic variations during seawater evaporation with fractional crystallization. *Chemical Geology: Isotope Geoscience section*, *86*(4), pp.323-333.

Ricardi-Branco, F. (2008). Venezuelan paleoflora of the Pennsylvanian-Early Permian: Paleobiogeographical relationships to central and western equatorial Pangea. *Gondwana Research*, *14*(3), 297-305.

Roberts, S. M., and **Spencer, R. J.** (1995). Paleotemperatures preserved in fluid inclusions in halite. *Geochimica et Cosmochimica Acta*, *59*(19), 3929-3942.

Schreiber, B.C. and **Kinsman, D.J.** (1975) New observations on the Pleistocene evaporites of Montallegro, Sicily and a modern analog. *Journal of Sedimentary Research*, **45**, 469-479.

Smoot JP, and **Castens-Seidel B** (1994) Sedimentary features produced by efflorescent salt crusts, Saline Valley and Death Valley, California. In: Renaut RW, Last WM (eds) Sedimentology and geochemistry of modern and ancient saline lakes, vol 50. SEPM (Society of Economic Paleontologists and Mineralogists), Tulsa, pp 73–90

Smoot, J.P. and **Lowenstein, T.K.** (1991) Depositional environments of non-marine evaporites. In *Evaporites, Petroleum and Mineral Resources* (Ed J. L. Melvin) *Developments in sedimentology*, 50, 189-347).

Sneh, A. (1983) Desert stream sequences in the Sinai Peninsula. *Journal of Sedimentary Research*, **53**, 1271-1279.

Southgate, P. N., Lambert, I. B., Donnelly, T. H., Henry, R., Etminan, H., & **Weste, G**. (1989). Depositional environments and diagenesis in Lake Parakeelya: a Cambrian alkaline playa from the Officer Basin, South Australia. *Sedimentology*, *36*(6), 1091-1112.

Stanesco, J.D. and **Campbell, J.A**. (1989) Eolian and noneolian facies of the lower Permian Cedar Mesa Sandstone Member of the Cutler Formation, southeastern Utah. *US Geol. survey bull.*; **1808, Chap. F.** Evolution of sedimentary basins-San Juan basin

Stanesco, J.D., Dubiel, R.F. and **Huntoon, J.E.** (2000) Depositional environments and paleotectonics of the Organ Rock Formation of the Permian Cutler Group, southeastern Utah. In*: Geology of Utah's Parks and Monuments* (Eds D.A. Sprinkel, T.C. Chidsey, Jr and P.B. Anderson), *Utah Geol. Assoc. Publ.*, 28, 591–605.

Stear, W.M. (1985) Comparison of the bedform distribution and dynamics of modern and ancient sandy ephemeral flood deposits in the southwestern Karoo region, South Africa. *Sedimentary Geology*, **45**, 209-230.

Szynkiewicz, A., Ewing, R.C., Moore, C.H., Glamoclija, M., Bustos, D. and **Pratt, L.M**.,(2010). Origin of terrestrial gypsum dunes—implications for martian gypsum-rich dunes of Olympia Undae. *Geomorphology*, ***121***(1-2), 69-83.

Taberner, C., Cendón, D., Pueyo, J. and **Ayora, C.,** (2000) The use of environmental markers to distinguish marine vs. continental deposition and to quantify the significance of recycling in evaporite basins. *Sedimentary Geology*, **137**, 213-240.

Tabor N.J. , Romanchock C.M. , Looy C.V. , Hotton C.L. , DiMichele W.A. , and **Chaney D.S. ,** (2013), Conservatism of Late Pennsylvanian vegetational patterns during short-term cyclic and long-term directional environmental change, western equatorial Pangea, in Gąsiewicz, A., and Słowokiewicz, M., eds., Palaeozoic Climate Cycles: Their Evolutionary and Sedimentological Impact : *Geological Society of London, Special Publications*, v. **376**, p. 201–234.

Tanner, L.H. and **Lucas, S.G.** (2007). The Moenave Formation: Sedimentologic and stratigraphic context of the Triassic–Jurassic boundary in the Four Corners area, southwestern USA. *Palaeogeography, Palaeoclimatology, Palaeoecology*, **244,** 111-125.

Thiemens, M. H. (2006). History and applications of mass-independent isotope effects. *Annu. Rev. Earth Planet. Sci.*, *34*, 217-262.

Thurston, R. S., Mandernack, K. W., and **Shanks III, W. C.** (2010). Laboratory chalcopyrite oxidation by Acidithiobacillus ferrooxidans: oxygen and sulfur isotope fractionation. *Chemical Geology*, *269*(3-4), 252-261.

Trudgill, B. D. (2011). Evolution of salt structures in the northern Paradox Basin: Controls on evaporite deposition, salt wall growth and supra-salt stratigraphic architecture. *Basin Research*, *23*(2), 208-238.

Tucker, M.E. (1978) Triassic Lacustrine Sediments from South Wales: Shore-Zone, Evaporites and Carbonates. In: *Modern and ancient lake sediments* (Eds A. Matter and M.E. Tucker), *International Association of Sedimentologists, Special Publication* 2, 205-224.

Tunbridge, I.P. (1981) Sandy high-energy flood sedimentation—some criteria for recognition, with an example from the Devonian of SW England. *Sedimentary Geology*, **28**, 79-95

Tunbridge, I.P., 1984. Facies model for a sandy ephemeral stream and clay playa complex; the Middle Devonian Trentishoe Formation of North Devon, UK. *Sedimentology*, 31(5), pp.697-715.

Turchyn, A. V., and **Schrag, D. P**. (2004). Oxygen isotope constraints on the sulfur cycle over the past 10 million years. *Science*, ***303***(5666).

Vackiner, A.A., Antrett, P., Stollhofen, H., Back, S., Kukla, P.A. and **Bärle, C..** (2011). Syndepositional tectonic controls and palaeo-topography of a permian tight gas reservoir in nw germany. *Journal of Petroleum Geology*, *34*(4), 411-428.

Vail, P.R., Audemard, F., Bowman, S.A., Eisner, P.N., and **Perez-Crus, C.** (1991) The stratigraphic signatures of tectonics, eustasy and sedimentology—an overview. In: *Cycles and Events in Stratigraphy* (Eds Einsele, G., Ricken, W., Seilacher A.), *Springer-Verlag, Berlin*. 617-659

Veiga, G.D., Spalletti, L.A. and **Flint, S.**, (2002). Aeolian/fluvial interactions and high-resolution sequence stratigraphy of a non-marine lowstand wedge: the Avilé Member of the Agrio Formation (Lower Cretaceous), central Neuquén Basin, Argentina. *Sedimentology*, *49*(5), pp.1001-1019.

Venus, J.H., Mountney, N.P. and **McCaffrey, W.D**. (2014) Syn-sedimentary salt diapirism as a control on fluvial-system evolution: an example from the proximal Permian Cutler Group, SE Utah, USA. *Basin Research*. 27(2), 152-182.

Waldeck, A.R., Cowie, B.R., Bertran, E., Wing, B.A., Halevy, I. and **Johnston, D.T**., (2019). Deciphering the atmospheric signal in marine sulfate oxygen isotope composition. *Earth and Planetary Science Letters*, *522*, pp.12-19.

Warke, M.R., Di Rocco, T., Zerkle, A.L., Lepland, A., Prave, A.R., Martin, A.P, Ueno, Y., Condon, D.J., and **Claire, M.W.,** (2020). The Great Oxidation Event preceded a Paleoproterozoic snowball Earth. *Proceedings of the National Academy of Sciences USA*, 117(24), 13314-13320.

Warren, J. K. (1991). Sulfate Dominated Sea-Marginal and Platform Evaporative Settings:: Sabkhas and Salinas, Mudflats and Salterns. In *Developments in Sedimentology* (Vol. **50**, pp. 69-187). Elsevier.

Warren, J. K. (2006). Evaporites: sediments, resources and hydrocarbons. Springer Science & Business Media.

Warren, J.K. (1983) Tepees, modern (southern Australia) and ancient (Permian—Texas and New Mexico)—a comparison. *Sedimentary Geology*, **34**, 1-19

Warren, J.K. (2016) Evaporites: A geological compendium. 2nd edn. Springer, Switzerland. 1783 pp.

Warren, J.K. and **Kendall, C.G.S.C.** (1985) Comparison of sequences formed in marine sabkha (subaerial) and salina (subaqueous) settings--modern and ancient. *AAPG Bulletin*, **69**, 1013-1023.

Wilkins, D. E., and **Currey, D. R.** (1997). Timing and extent of late Quaternary paleolakes in the Trans-Pecos closed basin, west Texas and south-central New Mexico. *Quaternary Research*, *47*(3), 306-315.

Wortmann, U. G., and **Paytan, A**. (2012). Rapid variability of seawater chemistry over the past 130 million years. *Science*, *337*(6092), 334-336.

Yung, Y.L., Lee, A.Y., Irion, F.W., DeMore, W.B. and **Wen, J.**, (1997). Carbon dioxide in the atmosphere: Isotopic exchange with ozone and its use as a tracer in the middle atmosphere. *Journal of Geophysical Research: Atmospheres*, *102*(D9), pp.10857-10866.

Zuchuat, V., Sleveland, A.R., Pettigrew, R.P., Dodd, T.J., Clarke, S.M., Rabbel, O., and **Midtkandal, I.,** (2019), Overprinted allocyclic processes by tidal resonance in an epicontinental basin: the Upper Jurassic Curtis Formation, east-central Utah, USA: *The Depositional Record*, **(5)** 272– 305.

FIGURE CAPTIONS

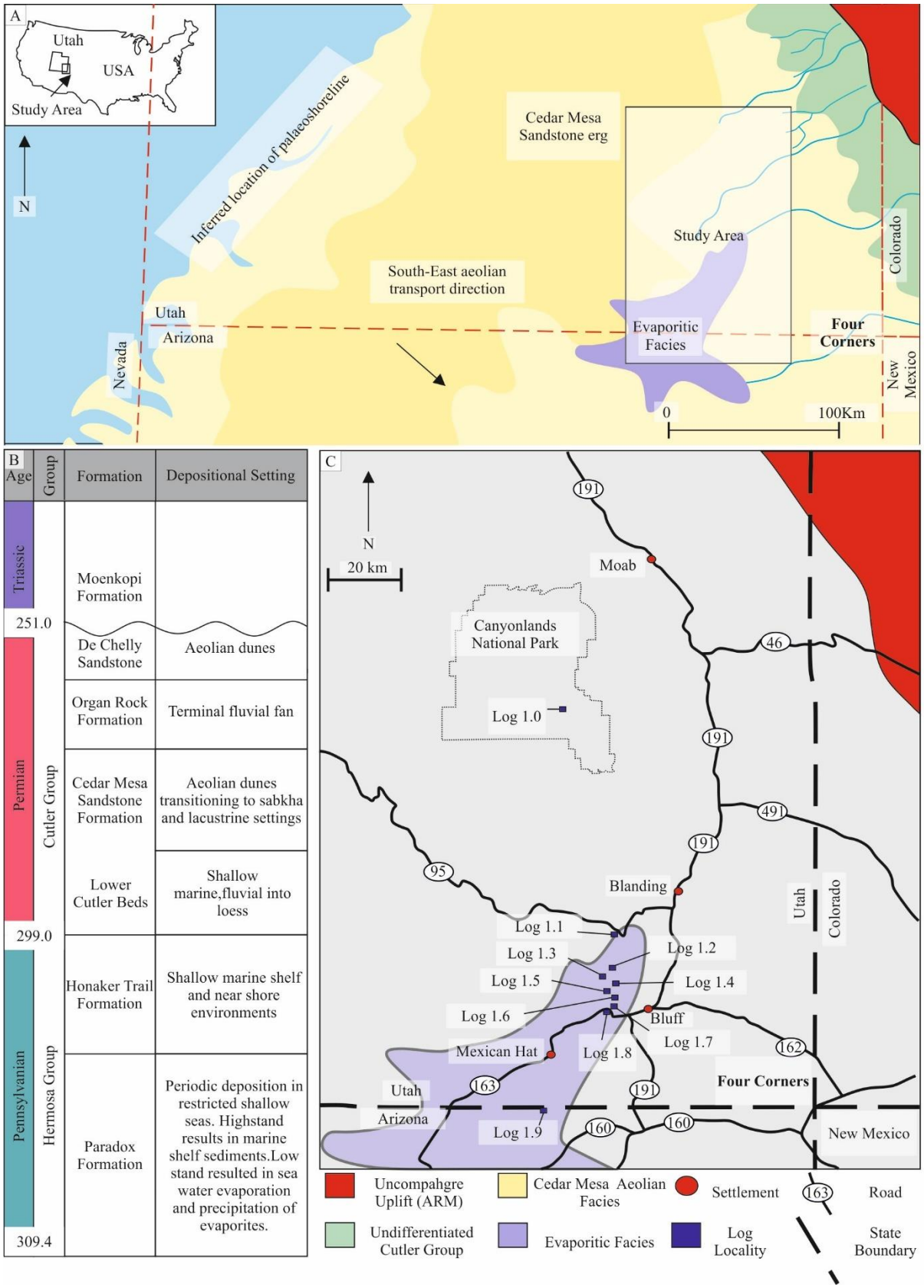

Figure 1 (**A)** Reconstructed paleogeography of the Cedar Mesa Sandstone Formation during the early Permian Period (after Blakey *et al.*, 1988). Location of the dune field is marked in dark yellow, with the location of evaporitic sediments shown in purple against an inferred land surface (light yellow). Present day state boundaries are superimposed and the study area is highlighted**. (B)** Stratigraphy of the study area from Pennsylvanian to Triassic times. Unconformities are marked with an undulating line (after Barbeau, 2003). (**C)** Study area and log localities pictured with roads, national parks and state boundaries. Palaeogeographical location of the sabkha facies (purple) and Uncompahgre Uplift (red) are also shown (after Blakey *et al.*, 1988).

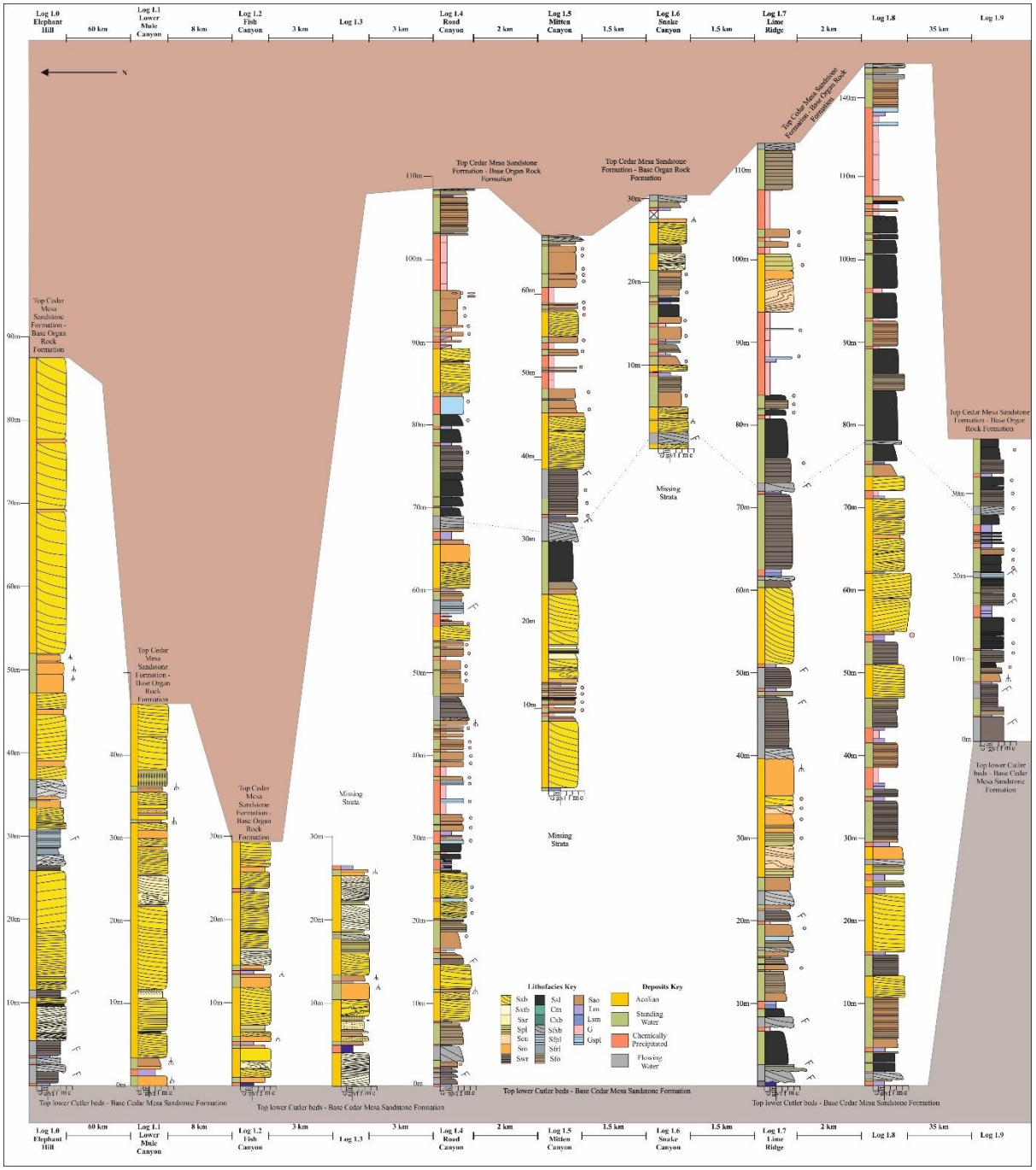

1317

1318 **Figure 2** Correlation of all logs within the study area. Logs are correlated from top of the lower Cutler
1319 beds to base of the Organ Rock Formation. Traceable units within the Cedar Mesa Sandstone Formation
1320 are shown with dashed lines. Logs are arranged along a roughly north – south transect. Distance between
1321 each log is shown. Lithofacies and deposit keys are shown in the figure.

1322 **Table 1** X-ray diffraction (XRD) sample numbers against log depth, with evaporite texture and XRD
1323 phases identified

Sample No.	Log Depth (m)	Evaporite Texture/Description	XRD phases identified
1	2	Vein within sandstone	gypsum, quartz, anhydrite
2	3	Nodule	gypsum, quartz, boracite
3	5	Vein within saline pan	gypsum, quartz, celestite
4	7.5	Vein	gypsum, quartz
5	12.5	Vein	gypsum
6	16	Interbedded with limestone	gypsum, quartz, anhydrite
7	16	Nodule within palaeosol	gypsum, quartz, anhydrite, magnesian calcite, feldspar
8	21	Vein within sandstone	gypsum, quartz
9	26.5	Interbedded gypsum and limestone	gypsum, quartz, rutile
10	27	Massive	gypsum
11	28	Massive	gypsum
12	30	Massive	gypsum, quartz
13	33.5	Enterolithic growth	gypsum, anhydrite
14	35.5	Enterolithic growth	gypsum, quartz, calcite
15	39.5	Massive	gypsum, anhydrite
16	42	Tepee structure	gypsum, quartz
17	42.5	Massive	gypsum, quartz, anhydrite
18	43	Massive	gypsum, quartz, anhydrite

19	43	Massive	gypsum, quartz
20	49	Interbedded with sandstone	gypsum, quartz, calcite
21	50	Interbedded with sandstone	gypsum, quartz, potassium sulfate
22	51.5	Interbedded with sandstone	gypsum, quartz
23	55.5	Massive	gypsum, quartz
24	65	Nodule within interdune sandstone	gypsum, quartz
25	66	Nodule within palaeosol	gypsum, quartz
26	70	Nodule	gypsum, quartz, boracite
27	70	Nodule	gypsum, quartz, anhydrite
28	89.5	Nodule within saline pan	gypsum, quartz, rutile
29	91.5	Nodular gypsum	gypsum anhydrite, muscovite
30	96.5	Massive	gypsum, celestite
31	97	Massive	gypsum
32	97.5	Massive	gypsum
33	98.5	Massive	not determined
34	99.5	Massive	gypsum
35	101	Massive	gypsum
36	102.5	Massive	gypsum

Table 2 Lithofacies of the Cedar Mesa Sandstone Formation

Facies	Code	Lithology	Sedimentary Structures	Interpretation

Planar cross-bedded sandstone	Sxb	Grey to orange, fine to medium-grained, well sorted & well rounded sandstone.	Planar cross-bedding with mm/cm scale alternations in grainsize occurring in single or multiple sets <10 cm, with localised soft sediment deformation.	Alternating laminations of grain fall and flow and migration of wind-blown straight-crested dune-scale bedforms and dune trains. Soft sediment deformation formed as a result of slumping of dune lee slope and/or haloturbation.
Trough cross-bedded sandstone	Stxb	Grey to orange, fine to medium-grained, well sorted & well rounded, sandstone.	Trough cross-bedding with mm/cm scale alternations in grainsize occurring in single or multiple sets.	Alternating laminations of grain fall and flow and migration of wind-blown sinuous-crested dune-scale bedforms and dune trains.
Ballistic ripple Sandstone	Sxr	Yellow, orange to white, fine to medium-grained, well sorted, sub to well–rounded, sandstone.	Horizontal laminations with bimodal sorting (pinstripe) with sporadic shallowly climbing (<8°) rippleform laminae.	Saltation of fine-grained sand, which accumulates along the saltation wavelength. Reptation of coarser grains over accumulated grains, results in inverse grading. Rippleform present where grain-size differentiation enables internal foreset laminae to be distinguished.
Structureless Sandstone	Sm	Grey to orange, fine to medium-grained, well sorted & well rounded, sandstone.	Structureless with localised desiccation cracks and root traces (rhizoliths).	Rapid suspension settling of wind-blown sediment in areas affected by surface water, followed by drying.
Plane parallel laminated to oscillatory current rippled siltstone and sandstone	Swr	Dark brown siltstone-to fine-grained moderately sorted & sub-rounded, siltstone and sandstone.	Parallel laminations with a sporadic undulose texture and symmetrical cross lamination.	Low energy, sub-aqueous setting, where the deposits have settled out of suspension. Undulose and oscillation-current ripples form in response to wind action on shallow waters.
Fine-grained carbonate	Lm	Dark grey to blue, carbonate mudstone/wackestone.	Sporadically blocky or stylotised with sporadic ostracod microfossils and nodular red microcrystalline chert.	Sub-aqueous precipitation of carbonate. The high matrix-content reflects a low energy in the system at the time of deposition.
Clastic-rich carbonate	Lsm	Dark grey to blue carbonate wackestone/ packstone with >10% fine grained sand within a carbonate mud matrix.	Sporadically blocky or stylotised.	Sub-aqueous precipitation of allochthonous carbonate with siliciclastic input from neighbouring environments. The lower proportion of matrix with respect to Facies Lm reflects slightly higher energy in the system at the time of deposition.

Gypsum	G	White to peach crystalline gypsum.	Massive or laminated bands of enterolithic convoluted folds or polygonal hummocks.	Precipitation from shallow saline waters and displacive growth of evaporites within saline saturated sediment.
Gypsum-bound sandstone	Gspl	Light grey, very fine to fine-grained, moderate to poorly sorted, sub-rounded sandstone within a gypsiferous matrix and cement.	Parallel laminated to massive, often contorted by small gypsum nodules.	Flow of saline fluid and subsequent precipitation of gypsum in the pore space as water evaporated at the ground surface.
Horizontally laminated mudstone and siltstone (Damp Pedogenic)	Sfo	Purple to light brown, silt to fine-grained, mudstone and siltstone.	Fining upwards horizontal laminations, mottled.	Vegetation stabilisation and sediment binding; product of palaeosol Presence of primary sedimentary features indicates a relatively immature palaeosol most likely in proximity to fluvial channels or confined bodies of water
Structureless Fines mudstone and siltstone (Dry Pedogenic)	Sfr	Light brown, grey to yellow very fine to fine-grained, moderately to well-sorted, sub-rounded mudstone and siltstone.	Structureless, sporadic gypsum and calcrete nodules and veins.	Vegetation stabilisation and sediment binding; product of palaeosol development.
Parallel laminated siltstone and sandstone	Ssl	Dark brown to black, siltstone to very fine-grained sandstone,	Structureless to faint parallel-laminations with normal grading and high organic content. sporadic mottling	Suspension fall out within low energy waters. High organic content indicates either thermal stratification or anoxic conditions.
Planar cross-bedded sandstone	Sfxb	Brown medium-grained moderately sorted & sub-rounded sandstone.	Planar cross-bedding with normal grading, in single or multiple sets, sporadic mud clasts.	Migration of straight-crested dune-scale bedforms and dune trains sub aqueously under lower flow regime conditions.
Plane parallel-stratified sandstone	Sfpl	Grey to brown, fine to medium-grained, moderately sorted, sub-rounded, sandstone	Plane parallel-stratification	Plane beds deposited under upper-flow regime conditions.
Climbing-ripple laminated sandstone	Sfrl	Grey to brown, fine to medium-grained, moderately sorted, sandstone	Sub-critically climbing asymmetrical cross-lamination	Lower flow regime ripple– scale bedform migration.

1326

1327

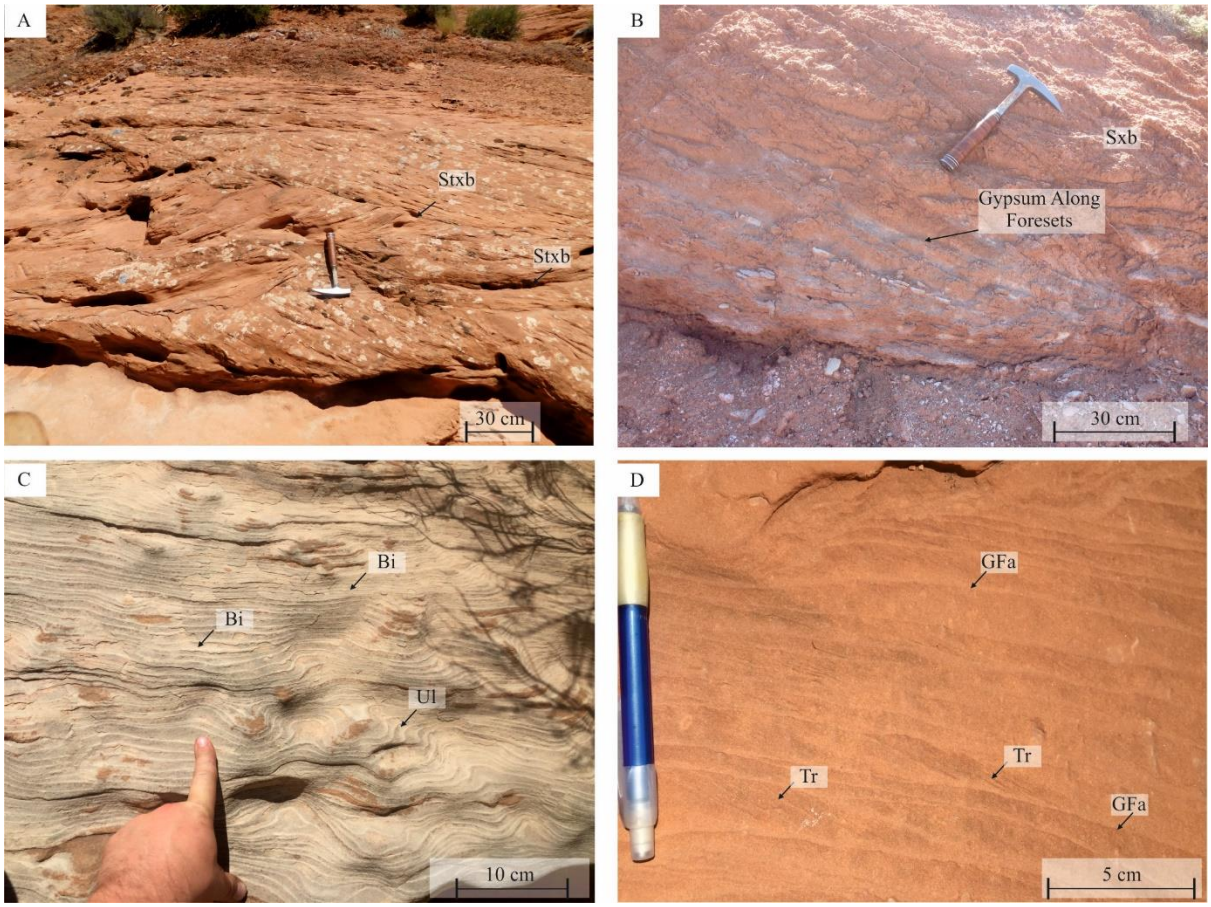

Figure 3 Key features of aeolian sediments. (**A)** Small trough cross bedding (Stxb) highlighted with arrow. (**B)** Gypsum rich dune facies (Sxb) with white gypsum alone bounding surfaces (arrowed). (**C)** Ballistic ripple sandstone (Sxr) with bimodal sorting (Bi arrowed) and undulating laminations (Ui arrowed). (**D)** Ballistic ripple sandstone (Sxr) with shallowly climbing rippleform laminae (Tr arrowed) between grainfall deposits (Gfa arrowed)

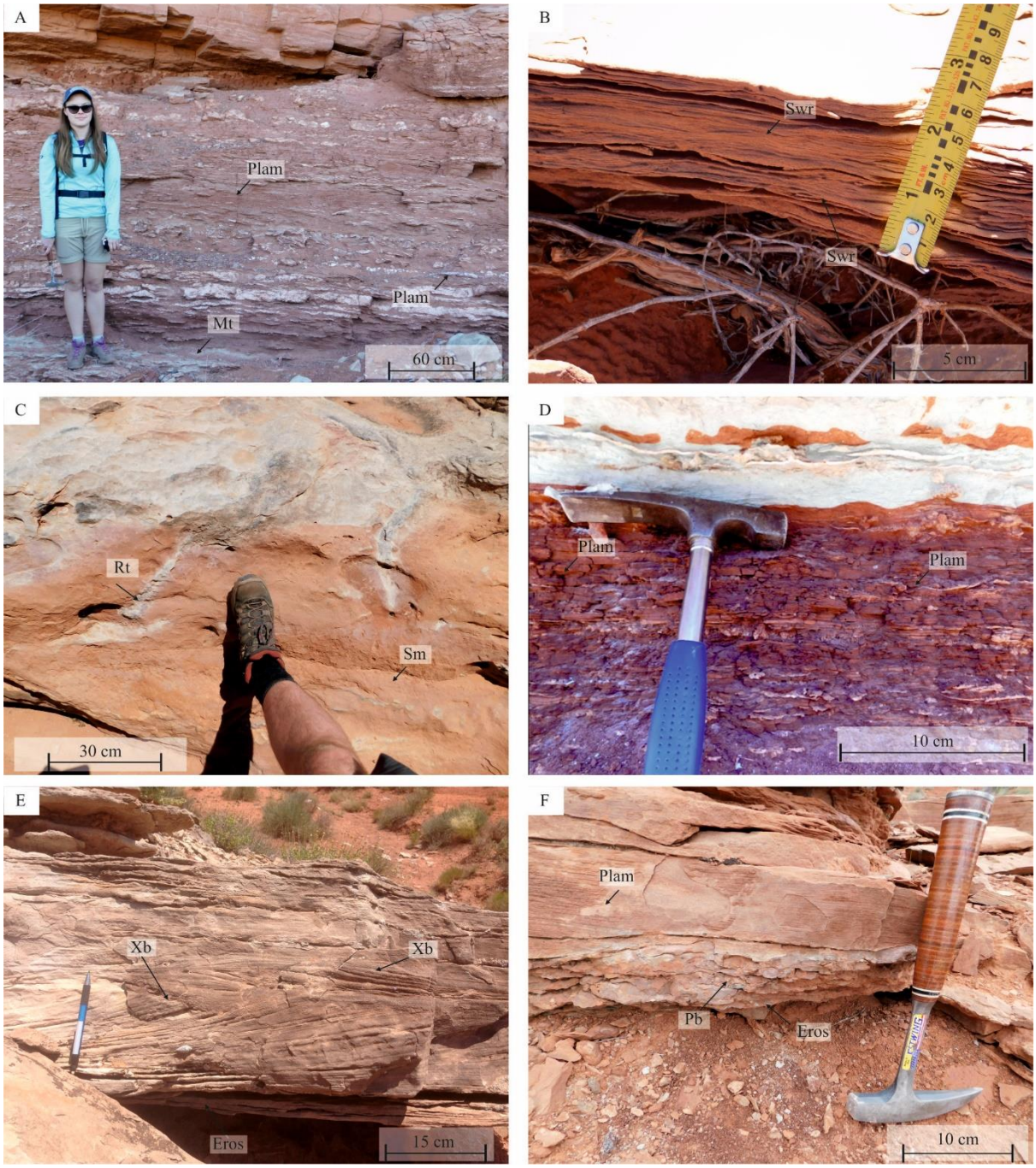

Figure 4 The key features of standing water (A) to (D) and flowing water deposits (E) and (F). (**A)** Parallel laminated siltstone and sandstone (Ssl) with planar laminations (Plam arrowed) and mottled appearance (Mt arrowed). (**B)** Plane parallel laminated to oscillation-current rippled siltstone and sandstone (Swr). (**C)** Structureless Sandstone (Sm) with root traces (Rt arrowed). (**D)** Horizontally laminated mudstone- and siltstone (Sfo) with parallel laminations (Plam arrowed). (**E)** Planar cross-bedded sandstone (Sfxb) with multiple cross-bedded sets (Xb arrowed) and erosional base (Eros). (**F)**

Plane parallel-stratified sandstone (Sfpl) overlying thin beds of Sfxb with mud clasts (Pb arrowed) and erosional base (Eros)

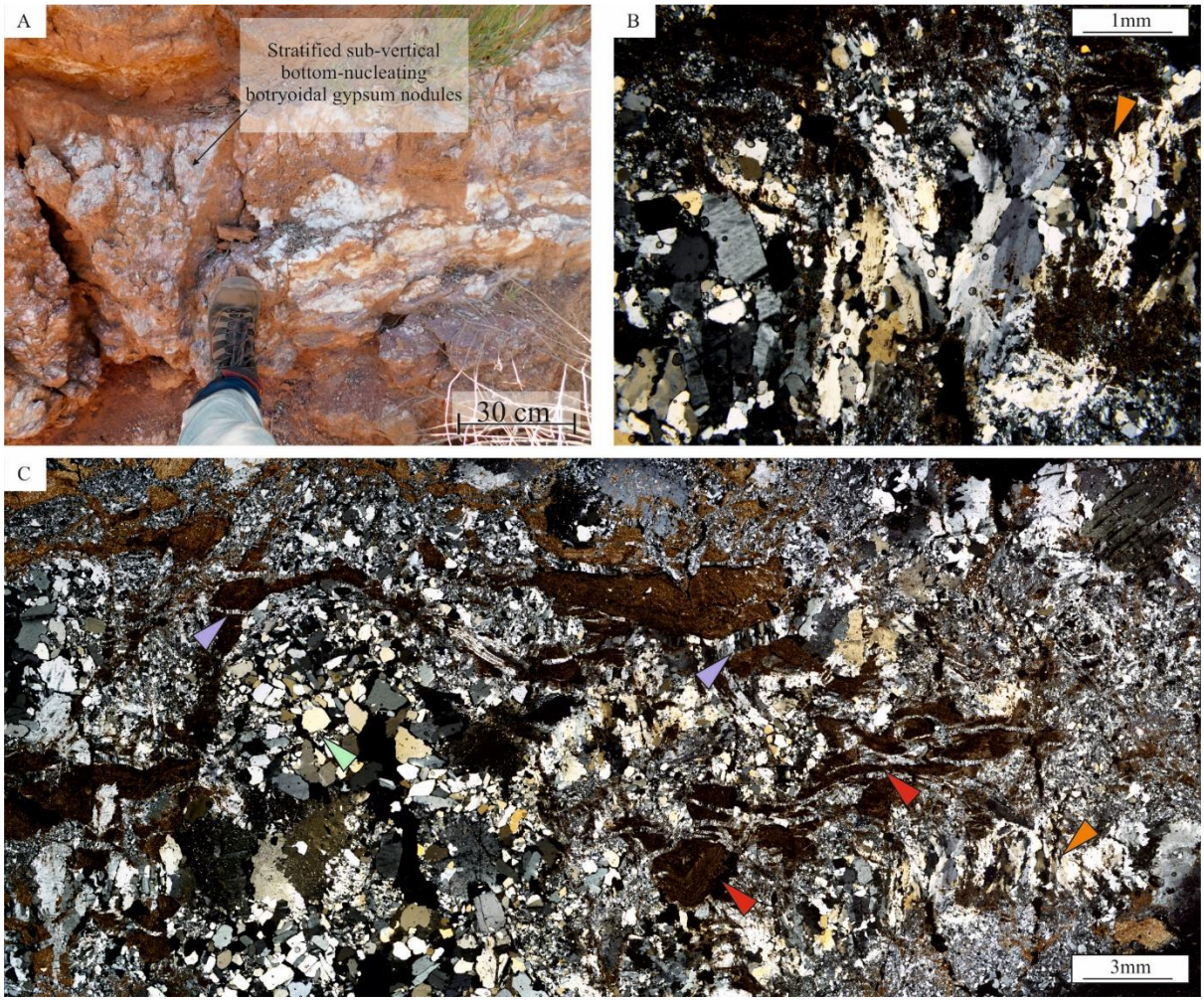

Figure 5 Key features of bedded gypsum/anhydrite deposits. (**A)** Bottom growing botryoidal nodules. (**B)** Thin section showing undulating beds of bladed gypsum with vertical textures (orange arrow). (**C)** This section showing alabastrine matrix of gypsum with: quartz sand grains (green arrow), undulating bladed vertical gypsum (orange arrow), veins filled with satin spar (purple arrow) and brown mud clasts (red arrow).

Figure 6 Key features of displacive gypsum/anhydrite deposits. (**A)** Tepee structure (Tp arrow) formed within gymsum (G). (**B)** Chicken wire texture in gypsum (G). (**C)** Enterolithic gypsum folds (arrowed) in background gypsum (G). (**D)** Multiple enterolithic folds in bed of gypsum (G). (**E)** Thin section showing poroproplastic gypsum matrix (orange arrow) with multiple diagenetic displacive halite crystals (red arrow) bladed gypsum cement crystals (yellow arrow) and mud clasts (green arrow).

Figure 7 Key features of brecciated gypsum/anhydrite deposits: (**A)** massive and slumped appearance in outcrop of gypsum (G); (**B)** crudely cross-bedded appearance of massive brecciated gypsum (G); (**C)** this section showing elongate gypsum crystals (orange arrow) and rounded edges (red arrow)

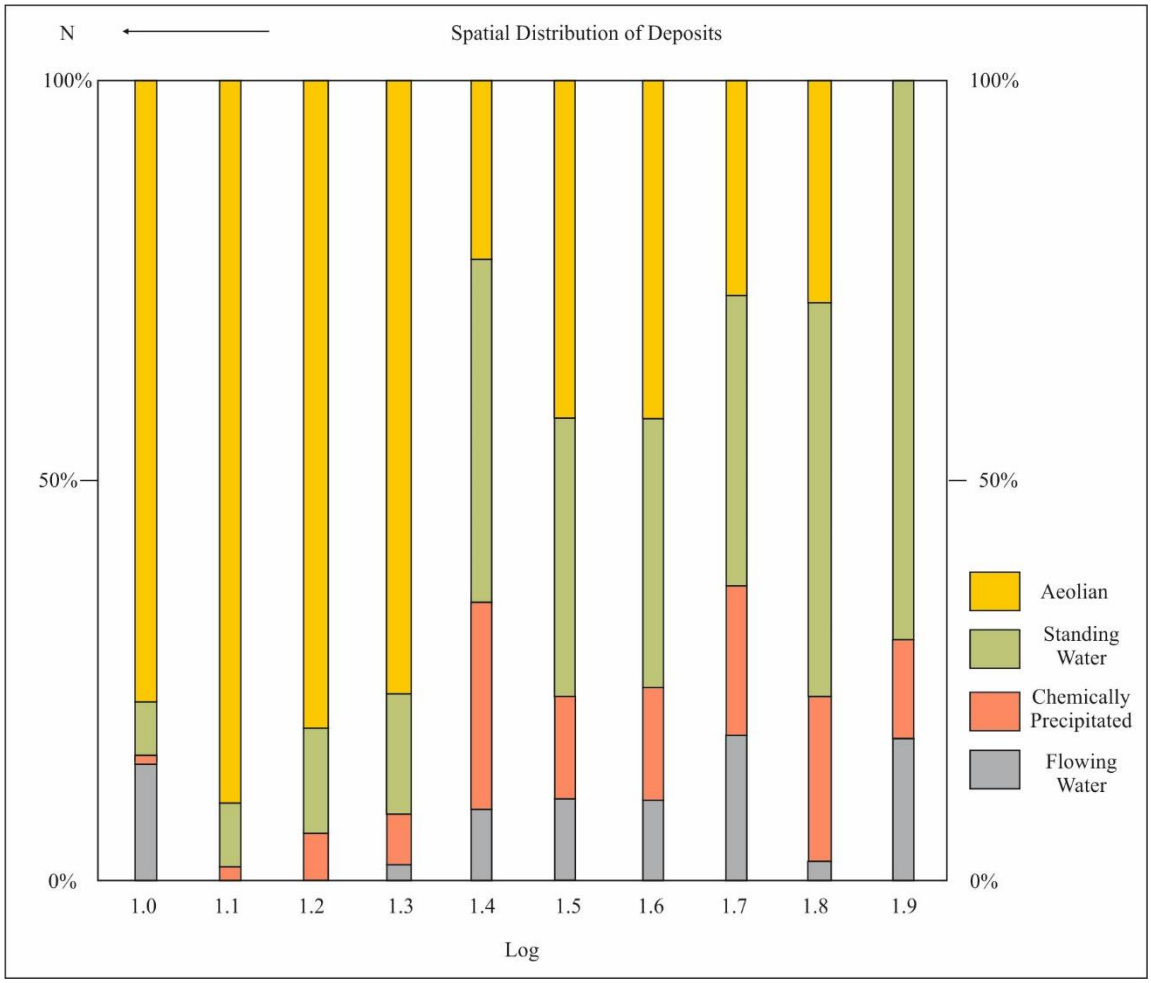

1359

1360 **Figure 8** Plot of relative proportions of aeolian, standing water, chemically precipitate and flowing
1361 water deposits in each log across the study area. Log number is shown along the bottom (see Fig. 1 for
1362 location) with percentage of each within each log plotted along the vertical axis.

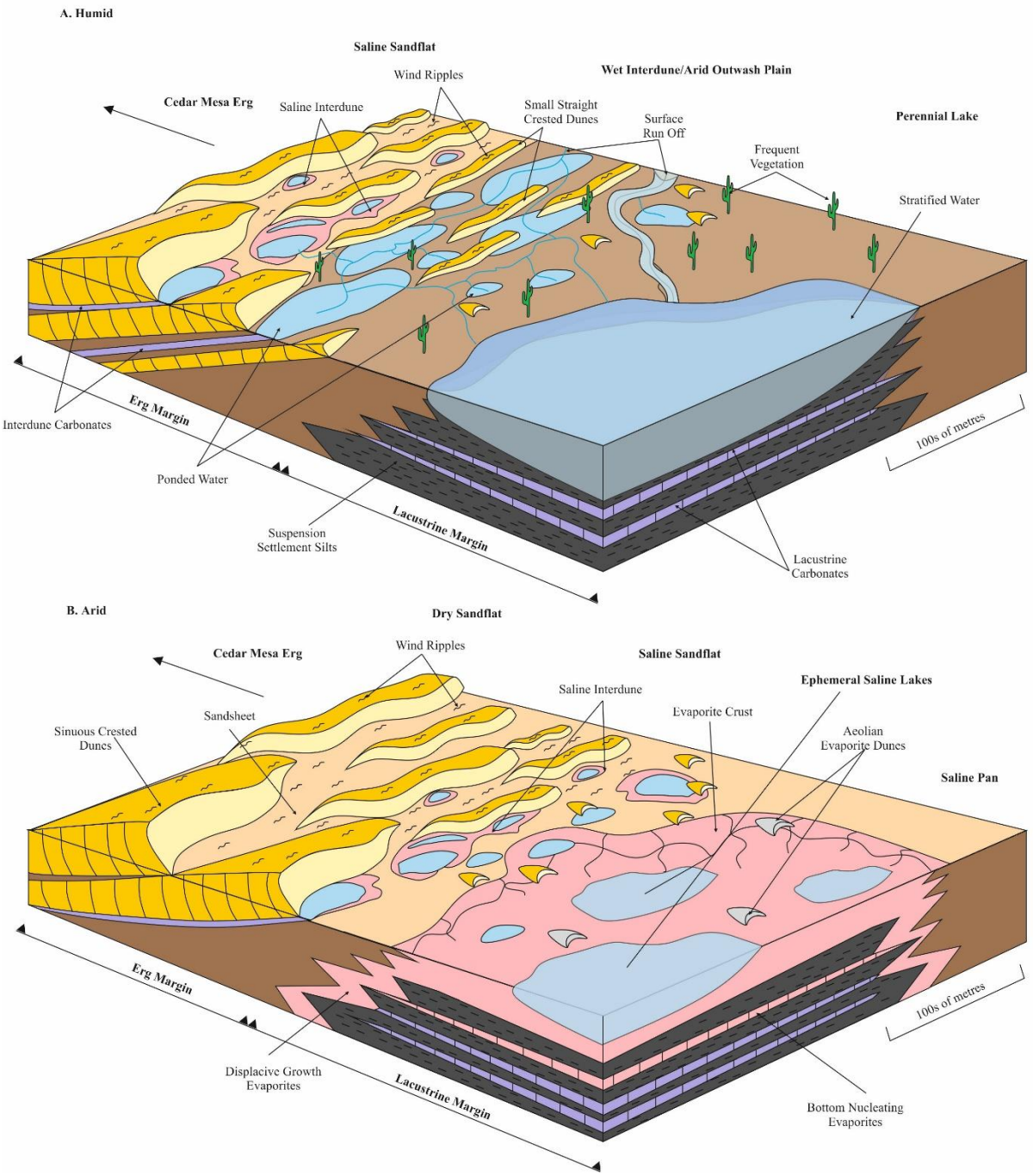

1363

1364 **Figure 9** Depositional models showing the sedimentology and depositional settings of either the erg
1365 margin or lacustrine margin setting during either humid (A) or arid (B) times.

1366 **Table 3** $\delta^{34}S$, $\delta^{18}O$ and $\Delta^{17}O$ measurements of gypsum/anhydrite samples from Log 1.4.

Sample No.	Depth (m)	$\Delta^{17}O$	error $\Delta^{17}O$	$\delta^{18}O$	Error $\delta^{18}O$	$\delta^{34}S$	Error $\delta^{34}S$

1	2	-0.13	0.02	15.46	0.50	14.29	0.30
2	3	-0.06	0.01	14.35	0.50	13.94	0.30
4	7.5	-0.26	0.22	n.d.	n.d.	13.73	0.30
5	12.5	-0.22	0.01	14.27	0.50	14.00	0.30
6	16	-0.20	0.04	16.69	0.50	14.00	0.31
9	26.5	-0.23	0.06	n.d.	n.d.	13.80	0.30
10	27	-0.09	0.03	15.18	0.50	13.88	0.30
11	28	-0.13	0.07	16.32	0.50	13.55	0.30
12	30	-0.22	0.03	15.79	0.50	13.87	0.30
13	33.5	-0.27	0.04	15.66	0.50	14.62	1.14
15	39.5	-0.27	0.01	n.d.	n.d.	13.93	0.30
16	42	-0.20	0.02	14.50	0.50	14.03	0.36
17	42.5	-0.09	0.02	14.46	0.50	13.92	0.30
18	43	-0.22	0.04	14.18	0.50	13.57	0.38
19	43	-0.15	0.02	14.18	0.50	13.43	0.30
20	49	-0.10	0.02	13.89	0.50	13.90	0.30
22	51.5	-0.23	0.04	12.80	0.50	n.d.	n.d.
23	55.5	-0.08	0.03	15.66	0.50	14.53	0.30
24	65	-0.16	0.02	15.02	0.50	14.33	0.30

26	70	-0.20	0.02	15.56	0.50	14.22	0.30
27	70	-0.16	0.02	15.19	0.50	14.39	0.30
28	89.5	-0.12	0.02	14.33	0.50	13.89	0.30
29	91.5	-0.15	0.00	15.05	0.50	13.88	0.30
31	97	-0.19	0.03	15.53	0.50	14.02	0.30
32	97.5	-0.13	0.02	15.48	0.50	14.50	0.30
33	98.5	-0.09	0.02	14.28	0.50	13.82	0.30
34	99.5	-0.19	0.04	15.37	0.50	14.38	0.30
35	101	-0.14	0.01	13.49	0.50	13.72	0.30
36	102.5	-0.14	0.00	13.82	0.50	13.74	0.30

1367

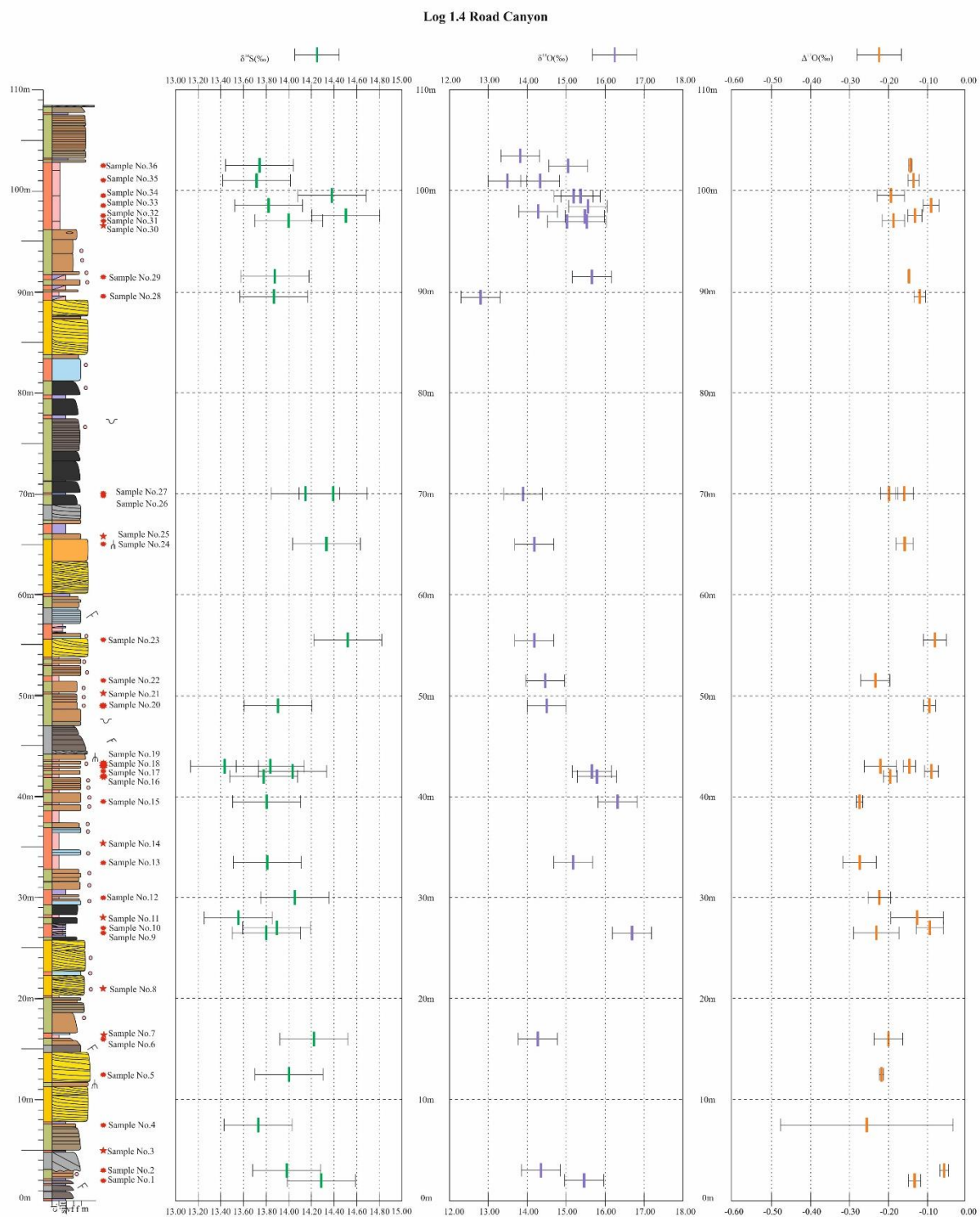

Figure 10 Isotope results plotted against log 1.4. $\delta^{34}S$ is plotted in green with error bars, $\delta^{18}O$ is plotted in purple with error bars. $\Delta^{17}O$ is plotted in orange with error bars. Red circle next to sedimentary log indicates sample location of isotopic and XRD data point, star indicates XRD sample only. For sedimentary facies key see Fig. 2.

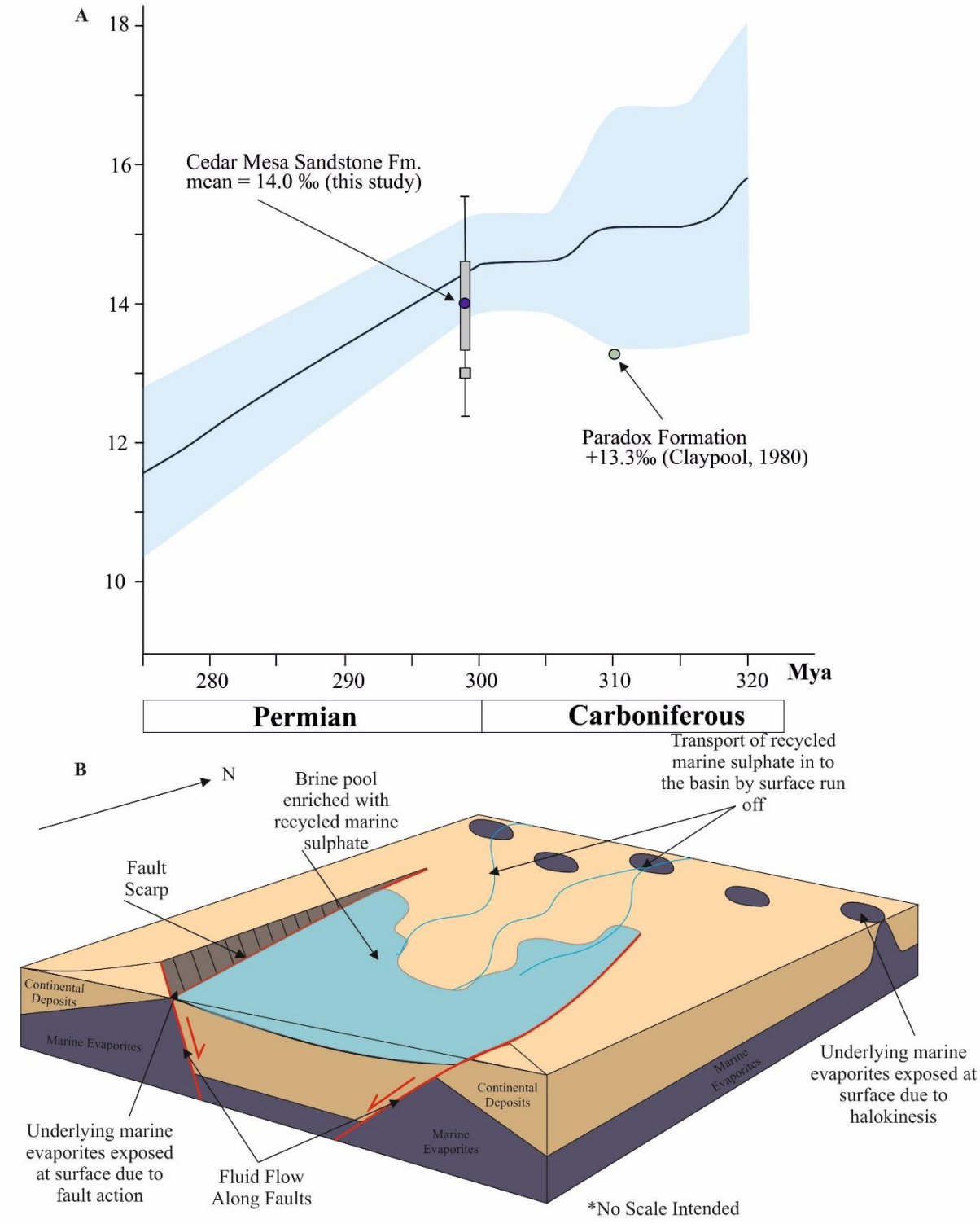

1373

1374 **Figure 11 (A)** Mean $\delta^{34}S$ of the Cedar Mesa Sandstone and Paradox Formation plotted against marine
1375 range during the Carboniferous and Permian (blue) (after Kampschulte & Strauss, 2004). (**B)** Schematic
1376 diagram showing possible pathways for marine sulphate flux into the continental basin via fault action,
1377 or through halokinesis and surface run off.

1378